Large-Eddy Simulation of a Water Jet Exhausting into Quiescent Air

Valentin Morin[*] and Julien Troyes[†]
ONERA, University of Toulouse, F-31055 Toulouse, France
François Vuillot[‡]
ONERA, University of Paris-Saclay, F-91123 Palaiseau, France
and
Christophe Bogey[§]
Laboratoire de Mécanique des Fluides et d'Acoustique, LMFA, UMR 5509, 69130 Ecully, France

This study focuses on a water injection system, typical of those used to inject water in the motor jet plume of rocket engines to reduce noise, and particularly on the destabilization of the liquid jet that leads to a spray system. For that purpose, a large-eddy simulation is conducted for an experimental water jet of the literature. It is a sprinkler whose Reynolds number is $Re = 82,000$ and nozzle exit diameter is $D = 4.37$ mm, similar to injectors used for jet noise reduction studies at a reduced scale. A diffuse interface method is used to calculate the dense liquid phase, and the dispersed phase containing droplets is calculated with an Eulerian solver. Transfers between the dense and the dispersed phases are modeled in the coupling procedure, including the atomization and impingement processes. The jet mean radius and initial instability frequency are consistent with the experimental data, while the position of the jet transition varies with the fluctuation levels at the nozzle exit. The droplets are created in the shear layer and accumulate on the jet center when only the atomization process is considered. When also implemented, the impingement phenomenon, however, is shown to absorb the droplets before they reach the center.

Nomenclature

A_{cell}	=	cell area, m^2
$<A>$	=	mean jet radius, m
B	=	deviator of the resolved symmetric strain tensor
C	=	interface curvature, m^{-1}
C_d	=	drag coefficient
C_S	=	Smagorinsky constant
c	=	speed of sound in water at 300 K, $\text{m} \cdot \text{s}^{-1}$
c_p	=	specific heat capacity at constant pressure, $\text{J} \cdot \text{K}^{-1} \cdot \text{kg}^{-1}$
D	=	nozzle exit diameter, m
D_g	=	gas diffusion coefficient, $\text{m}^2 \cdot \text{s}^{-1}$
D_l	=	liquide diffusion coefficient, $\text{m}^2 \cdot \text{s}^{-1}$
D_t	=	turbulent diffusion coefficient, $\text{m}^2 \cdot \text{s}^{-1}$
D_{lig}	=	ligament equivalent diameter, m
e_t	=	total energy per unit of mass, $\text{J} \cdot \text{kg}^{-1}$
$\boldsymbol{F}$	=	flux vector
f	=	frequency, Hz
h	=	specific enthalpy, $\text{J} \cdot \text{kg}^{-1}$
I	=	identity tensor
I_c	=	synthetic-eddy method intensity coefficient
I_B	=	double dot product of the deviator of the resolved symmetric strain tensor
J	=	molecular diffusive flux, $\text{kg} \cdot \text{m}^{-2} \cdot \text{s}^{-1}$
$\boldsymbol{J}_e$	=	heat flux, $\text{W} \cdot \text{m}^{-2}$
k	=	wave number, m^{-1}
l_w	=	distance from the wall, m
m	=	mass, kg
N	=	number of turbulent spots
n	=	probability density function of droplet number
Oh	=	Ohnesorge number
PSD	=	power spectral density
p	=	static pressure, Pa
Q	=	Q criterion
$\boldsymbol{Q}$	=	vector of conservative variables
R	=	distance of the interface from the center axis, m
Re	=	Reynolds number
r	=	radial distance to the center axis, m
r_g	=	specific gas constant, $\text{J} \cdot \text{kg}^{-1} \cdot \text{K}^{-1}$
S	=	mass transfer per unit of volume and time, $\text{kg} \cdot \text{m}^{-3} \cdot \text{s}^{-1}$
$\boldsymbol{S}$	=	exchange term vector between the dense phase solver and the dispersed phase solver
St	=	Strouhal number
s	=	curvilinear abscissa, m
T	=	static temperature, K
TKE	=	turbulent kinetic energy, $\text{J} \cdot \text{kg}^{-1}$
Tu	=	turbulence intensity
U	=	velocity magnitude, $\text{m} \cdot \text{s}^{-1}$
$\boldsymbol{U}$	=	velocity vector, $\text{m} \cdot \text{s}^{-1}$
u''	=	fluctuating velocity magnitude, $\text{m} \cdot \text{s}^{-1}$
V_{box}	=	volume of the synthetic-eddy method box, m^3
V_{cell}	=	volume of a cell, m^3
We	=	Weber number
X	=	axial distance to the nozzle exit, m
$\boldsymbol{X}_k$	=	position of the center of the spot k
x, y, z	=	spatial coordinates
Y	=	mass fraction
α	=	volume fraction
α_0	=	liquid isobaric dilatation coefficient
β_0	=	liquid isothermal compressibility
γ	=	surface tension coefficient, $\text{N} \cdot \text{m}^{-1}$
Δ	=	grid cutoff, m
Δt	=	simulation time step, s

*Ph.D. Student, Multi-Physics for Energetics Department; valentin.morin@onera.fr.
†Research Scientist, Multi-Physics for Energetics Department; julien.troyes@onera.fr.
‡Research Scientist, Multi-Physics for Energetics Department; francois.vuillot@onera.fr.
§CNRS Research Scientist, University of Lyon, Ecole Centrale de Lyon, Institut National des Sciences Appliquées de Lyon, University Claude Bernard Lyon I; christophe.bogey@ec-lyon.fr. Associate Fellow AIAA.

δ_{grid}	=	grid size, m
δ_v	=	vorticity-layer thickness, m
ϵ	=	random coefficient -1 or 1 and turbulent dissipation rate, $m^2 \cdot s^{-3}$
κ	=	Von Kàrmàn constant
λ	=	wavelength, m
λ_a	=	atomization activation function
λ_i	=	impingement activation function
λ_T	=	thermal conductivity, $W \cdot m^{-1} \cdot K$
μ	=	dynamic viscosity, Pa·s
ν	=	kinematic viscosity, $m^2 \cdot s^{-1}$
ρ	=	density, $kg \cdot m^{-3}$
σ	=	size of a turbulent spot, m
τ	=	stress tensor

Subscripts

a	=	atomization
C	=	convective
c	=	at the center, capillary
D	=	diffusive
d	=	droplet
$dense$	=	dense phase solver
dis	=	dispersed phase solver
ej	=	conditions at the nozzle exit
g	=	gas
i	=	impingement and instability
i, j	=	tensor coordinates
inj	=	conditions at the water inlet
l	=	liquid
RT	=	Rayleigh–Taylor
SGS	=	subgrid Smagorinsky model
t	=	turbulent
th	=	theoretical
$1/2$	=	half-width

I. Introduction

FOR a space launcher, the noise [1] generated by the jet engines induces unsteady stresses on the rocket, its payload, and the launch pad. When the jet is supersonic, several noise components are emitted. Among them, there are turbulent mixing noise [2], as for subsonic jets, but also Mach waves generated by supersonic convective structures [3], broadband-shock-associated-noise [4,5], and possibly screech noise [6] coming from shock and turbulence interactions. Research has been made for many years to reduce the acoustic levels or at least to lower their damaging effects. In particular, injecting large quantities of water in the motor jet plume was found to effectively decrease the jet noise levels [7–9]. The hot and fast exhaust gas transfers momentum and heat to the droplets of the spray formed by water injection devices, leading to acoustic power loss. However, the interaction mechanisms between droplets and turbulent structures in the mixing layer of a gas jet remain unclear. To better understand these mechanisms, the droplet characteristics such as their size, velocity, and mass fraction have to be identified. When water exhausts from a nozzle, the transition between the dense phase regime where the liquid and gas are clearly separated and the dispersed phase containing droplets is called atomization. This phenomenon consists of multiple processes. In the first one, the shear at the liquid–gas interface generates Kelvin–Helmholtz (KH) instabilities [10–13] amplified due to the presence of a density gradient, a velocity gradient, and a surface tension. Then, for axisymmetric jets, azimuthal Rayleigh–Taylor (RT) instabilities emerge and trigger the breakup of the dense liquid phase into large ligaments [14,15]. This process is referred to as primary atomization. The ligaments break up into multiple droplets, which can themselves be fragmented into smaller droplets. This last process is referred to as secondary atomization. If the primary liquid breakup and the evolution of large liquid ligaments can be accurately solved by direct numerical simulation (DNS) [16,17] or large-eddy simulation (LES) [18,19], the secondary breakup and the generation of small droplets must be modeled.

Concerning the launch pad injection devices, the influence of parameters such as the injection angle, the distance to the nozzle exit, and the liquid mass flow rate of the water jets on noise reduction has been studied in several experimental works [7–9,20]. Simulations have also been performed [21–24] and focused on the modeling of the interactions between the water and the motor jet plume. The studies of Fukuda et al. [21], Capecelatro and Buchta [22], and Buchta et al. [23] considered the interactions between the droplets and the gas jet, and did not take into account the interactions between the water dense phase and the gas. In the work of Fukuda et al. [21], the sound power level of the noise suppression obtained using Reynolds-averaged Navier–Stokes (RANS) simulation was in good agreement with the experimental data, but the droplet size was arbitrarily set. Thus, the influence of the injector geometry and of the exit velocity on the droplet diameter could not be investigated. Capecelatro and Buchta [22] and Buchta et al. [23] implemented a DNS of a jet noise reduction with droplets, and obtained a good agreement of the sound pressure level with experimental results. Their calculation enabled to analyze the droplet behavior in the turbulent mixing layer, but cannot be conducted for a complex configuration with multiple water injectors. On the other hand, Salehian and Mankbadi [24] performed a high-fidelity simulation of the interactions between a water dense phase and a gas. They directly calculated the atomization of the largest droplets and ligaments using a volume-of-fluid method [25], but did not resolve the small droplets. In their simulation, if noise reduction was well predicted for low acoustic frequencies, noise suppression was overestimated for high frequencies. The droplets were too large due to the surface tension neglected in the model. The present work aims to use a hybrid method to calculate both the dense phase of the jet including surface tension effects and the simulation of the small droplets in the spray. In that way, the largest droplets can be calculated by a dense phase solver as in Salehian and Mankbadi [24], and the smallest droplets atomized after the breakup of ligaments are taken into account in a dispersed phase solver. The exchange area between the two phases as well as the momentum, heat, and mass transfers and consequently the noise reduction are thus expected to be accurately calculated. The present approach, by considering in the same simulation both the dense and dispersed liquid phases, will complement the previous computational works mentioned above.

The objective of the present study is to validate the numerical methodology for the simulation of the water nozzles used at the MARTEL bench [26], which is an experimental setup used to study jet noise at a reduced scale. As there is no experimental data about these nozzles, calculations are carried out for a sprinkler case [27,28] whose parameters correspond to those of the water injectors used for jet noise reduction experiments at the MARTEL bench [7,20]. The paper focuses on the simulation of the primary atomization process and the ligament breakup of the water jet. Fragmentation and coalescence of droplets are not taken into account. Two solvers from the CEDRE code developed at ONERA [29] are used for the simulation. The first one is a Navier–Stokes solver for the dense phase, using a diffuse interface method [30–34]. The evolution of the liquid mass fraction is calculated and the interface position can be estimated only from postprocessing results. It differs from front-tracking [35,36] or front-capturing [37,38] methods, where the interface geometry is directly resolved. These latter techniques are more accurate but also more difficult to implement in complex configurations and can suffer from mass nonconservation [39]. A synthetic-eddy method (SEM) based on the work of Jarrin et al. [40,41] and Jarrin [42] is also applied to seed the interface instabilities of the dense phase regime. The second solver is an Eulerian resolution of the dispersed phase based on the Williams–Boltzmann kinetic equations. Primary atomization of droplets is first calculated, and then simulation with atomization and re-absorption of droplets into the dense phase, called impingement in this study, is carried out in a second step. Atomization and impingement processes are modeled with mass, momentum, and energy transfers between the dense and dispersed phase solvers, according to the work of Le Touze [43] and Le Touze et al. [33].

The present paper is organized as follows. The experimental setup is first presented in Sec. II. Then, the numerical procedure, namely,

the dense and the dispersed phase solvers and the SEM, is described in Sec. III. In Sec. IV.A.1, a parametric study about the setup of the SEM is shown. Then the flow inside the nozzle and at its exit is studied in Secs. IV.A.2 and IV.A.3. The jet transition obtained by the simulation with the dense phase only is investigated in Sec. IV.B.1, where the instability frequency of the jet and the mean jet radius are compared to the experiment. Finally, results including the simulation with atomization of droplets, then with both atomization and impingement, are shown in Sec. IV.C.

II. Experimental Configuration

A. Experimental Setup

The configuration investigated is based on the water jet in the experiments of Stevenin [27] and Stevenin et al. [28]. The injector, depicted in Fig. 1, is the sprinkler RB46 designed for crop irrigation. It is composed of an elbow, a long slightly converging section with an angle of 1° containing four perpendicular stabilizing fins, followed by a 34° converging section and ended by a small cylindrical nozzle with an exit diameter of $D = 4.37$ mm.

The main characteristics of the regime of interest are given in Table 1. Four nondimensional numbers are defined to describe the jet. They indicate which phenomena have preponderant effects on the flow. The variable $U_{ej} = 24.37$ m $\cdot$ s^{-1} is the nozzle exit velocity, $U_g = 0$ m $\cdot$ s^{-1} is the gas velocity, ρ_g and ρ_l are the gas and liquid densities, ν_l and μ_l are the kinematic and dynamic viscosities of the liquid, and γ is the surface tension coefficient. The liquid Reynolds number $Re_l = U_{ej}D/\nu_l$ is the ratio between the fluid inertia forces

and the liquid molecular viscosity. It is equal to 82,000, revealing that molecular viscosity is negligible with respect to the inertia forces and that the jet is in a turbulent regime. The Weber number We compares the inertia forces with capillarity. Two definitions, $We_l = \rho_l(U_{ej} - U_g)^2D/\gamma$ and $We_g = \rho_g(U_{ej} - U_g)^2D/\gamma$, are given in Table 1 depending on whether the number is related to the liquid or to the gas phase. The first one is equal to 36,000 and the second one is equal to 43. The Ohnesorge number $Oh = \mu_l/\sqrt{\rho_l\gamma D}$ is the ratio between molecular viscosity and capillarity. Its value is 0.0023 for this jet.

Each nondimensional number taken individually does not give relevant information on the atomization regime but their combination does. For that, experimental diagrams based on the nondimensional numbers have been proposed by authors such as Reitz [44], Lasheras and Hopfinger [45], and Stahl et al. [46]. The liquid breakup regime of the present configuration stands between the "wind induced" and "atomization" regimes in these diagrams, indicating that the liquid breakup occurs a few diameters downstream of the nozzle exit and that the size of the droplets is smaller than the jet diameter [44].

B. Mesh and Boundary Conditions

The mesh and the assumptions used in the numerical model are presented in this section. To simplify the geometry, choice is made to replace the converging and the cylindrical sections of the nozzle by one cylindrical section of the same length $3.12D$ and diameter $D = 4.37$ mm. Therefore, the elbow, the converging section, and the stabilizing fins are not taken into account. The outside numerical domain is a large cylinder box, whose transverse cut is presented in Fig. 2a.
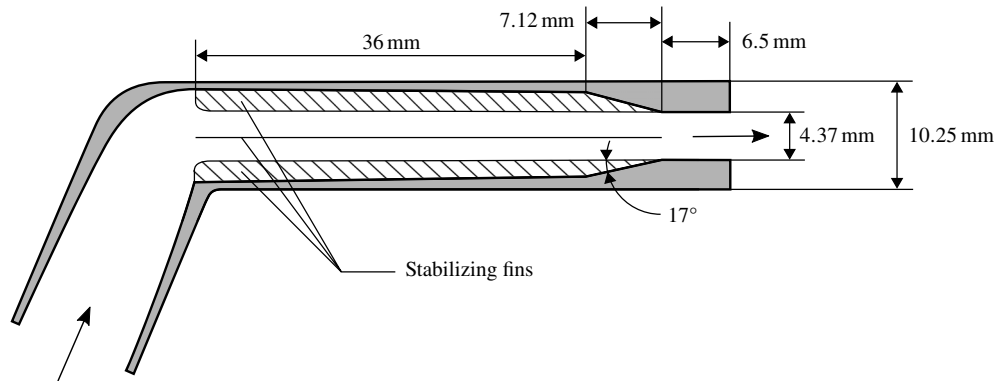

Fig. 1 Experimental water nozzle [27].

Table 1 Injector's parameters

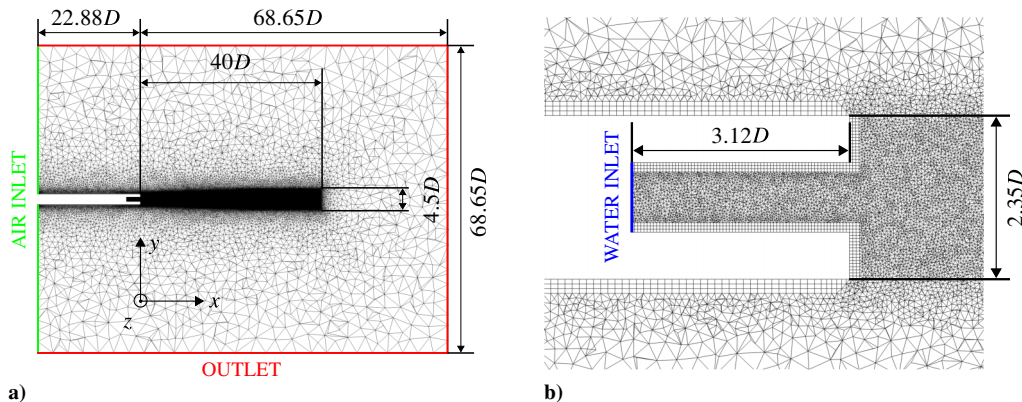| Variable	U_{ej}, m/s	Re_l	We_l	We_g	Oh
Definition	——	$U_{ej}D/\nu_l$	$\rho_l(U_{ej} - U_g)^2D/\gamma$	$\rho_g(U_{ej} - U_g)^2D/\gamma$	$\mu_l/\sqrt{\rho_l\gamma D}$
Value	24.37	82,000	36,000	43	0.0023

Fig. 2 Mesh representation: a) full mesh; b) zoom.

Table 2 Boundary conditions

Parameter	Prescribed variables	Species	U, m · s^{-1}	p, kPa	T, K
Air inlet	U, T	Air	2	——	294.15
Water inlet	U, T	Water	24.37, 27.62	——	294.15
Outlet in	U, T	Air	2	——	294.15
Outlet out	p	——	——	99.97	——

The boundary conditions are summarized in Table 2, where U, T, and p are, respectively, the velocity, the static temperature, and the static pressure. It should be pointed out that the velocity imposed at the inlet is uniform all over the boundary. Most of the simulations are conducted using the inlet velocity of $U_{ej} = 24.37$ m · s^{-1}, but one simulation with $U_{ej} = 27.62$ m · s^{-1} is also conducted in Secs. IV.B.2 and IV.B.3. A smooth coflow of a velocity of 2 m · s^{-1} is applied at the air inlet boundary in order to increase the robustness of the simulation. The outlet is automatically defined differently whether the fluid enters or exits the domain. When the fluid exits the domain, only pressure is imposed at the boundary. However, when the direction of the flow is oriented toward the domain, the velocity, the temperature, and the direction of the fluid are imposed at the boundary cells. For each boundary, other than prescribed variables are calculated to ensure continuity.

Simulations are carried out using the mesh presented in Fig. 2a, whose refined area is 40 diameters long, for two specific grid sizes $\delta_{grid} = 0.0229D$ and $\delta_{grid} = 0.0183D$, where $\delta_{grid} = 6 \times V_{cell}/A_{cell}$ is the equivalent cell diameter, with V_{cell} and A_{cell} being the volume and the area of a cell, in order to evaluate the influence of the mesh resolution on the results. The grid size is the same inside the injector and outside in the refined area extending from $X = 0$ down to $X = 40D$ and over $r \leq 2.35D$. Three layers of hexaedra are set on the walls, inside and outside the injector, to increase the robustness of the simulation. The finer mesh contains 28.2 million cells and the coarser one 15.4 million cells.

III.   Numerical Procedure

A.   Dense Phase Solver

The dense phase flow solver used is the CHARME solver from the CEDRE code developed at ONERA [29], based on the Navier–Stokes equation system for two species. This is a model where the fluid is considered locally homogeneous regarding velocity, pressure, and temperature. It is a simplification of the general model of Baer and Nunziato [47], based on a seven-equation formulation, which takes into account velocity, pressure, and temperature discontinuities between liquid and gas phases. This latter model is more complex to implement and is not retained in this work. The present model is a monofluid approach where liquid and gas mass fractions, and hence mean density, are calculated. Each cell is a mixture of the two phases and the liquid–gas interface is diffused in the mesh. Its position can be estimated from postprocessing results using special criteria. To perform LESs, the governing equations are filtered at the length scale $\Delta = \delta_{grid}$. The filtering operator is denoted as $\widehat{\cdot}$, and variables are expressed according to the Favre decomposition $\widetilde{\cdot}$ given by $\widetilde{\phi} = \widehat{\rho\phi}/\widehat{\rho}$ for any variable ϕ. The filtered variables computed in the solver are presented below.

The vector of conservative filtered variables is expressed by $\widehat{\boldsymbol{Q}} = (\widehat{\rho}\widetilde{Y}_l, \widehat{\rho}\widetilde{Y}_g, \widehat{\rho}\,\widetilde{\boldsymbol{U}}, \widehat{\rho}\,\widetilde{e}_t)^t$, where ρ is the mixture density; Y_l and Y_g are, respectively, the liquid and gas mass fractions; $\boldsymbol{U}$ is the velocity vector; and e_t is the total energy per unit of mass. The four governing equations, namely, the liquid and gas mass, the momentum vector, and the energy conservation, can be written as

$$\frac{\partial \widehat{\boldsymbol{Q}}}{\partial t} + \nabla \cdot \widehat{\boldsymbol{F}}_C = \nabla \cdot \left(\widehat{\boldsymbol{F}}_D + \widehat{\boldsymbol{F}}_t \right) - \widehat{\boldsymbol{S}}_{\textbf{dense}} \tag{1}$$

where S_{dense} denotes the exchange term between the dense phase solver and the dispersed phase solver when activated. Two phenomena are modeled. The first one is the atomization and corresponds to the generation of droplets from the dense phase, and the second one is the impingement of the droplets on the dense liquid phase. The exchange term is given by

$$\widehat{\boldsymbol{S}}_{dense} = \begin{pmatrix} S_a \\ 0 \\ n\boldsymbol{F}_d + S_a \widetilde{\boldsymbol{U}} - S_i \boldsymbol{U}_d \\ S_a \left(c_p(T_a) + \frac{1}{2}\widetilde{\boldsymbol{U}}^2 \right) - S_i \left(c_p(T_d) + \frac{1}{2} \boldsymbol{U}_d^2 \right) + n\boldsymbol{F}_d \cdot \boldsymbol{U}_d \end{pmatrix} \tag{2}$$

where $\boldsymbol{F}_d$ is the drag force of the droplets, S_a is the atomization mass transfer rate, S_i is the impingement mass transfer rate, c_p is the heat capacity of droplets at constant pressure, T_a is the initial temperature of the atomized droplets, $\boldsymbol{U}_d$ is their velocity, and T_d is their temperature. All these terms are detailed in Sec. III.B. The vectors $\widehat{\boldsymbol{F}}_C$ and $\widehat{\boldsymbol{F}}_D$ are, respectively, the convective and dissipative fluxes given by

$$\widehat{\boldsymbol{F}}_C = \widehat{\boldsymbol{Q}} \otimes \widehat{\boldsymbol{U}} + \widehat{p} \begin{pmatrix} 0 \\ 0 \\ I \\ \widetilde{\boldsymbol{U}} \end{pmatrix} \tag{3}$$

with I the identity tensor, and

$$\widehat{\boldsymbol{F}}_D = \begin{pmatrix} -\widehat{\boldsymbol{J}}_l \\ -\widehat{\boldsymbol{J}}_g \\ \widehat{\tau} - \widehat{\tau}_c \\ (\widehat{\tau} - \widehat{\tau}_c) \cdot \widetilde{\boldsymbol{U}} - \widehat{\boldsymbol{J}}_e \end{pmatrix} \tag{4}$$

The fluxes $\widehat{\boldsymbol{J}}_l$ and $\widehat{\boldsymbol{J}}_g$ are formulated by the Fick's laws :

$$\widehat{\boldsymbol{J}}_l = -\widehat{\rho}\widetilde{D}_l \nabla \widetilde{Y}_l \tag{5}$$

$$\boldsymbol{J}_g = -\widehat{\rho}\widetilde{D}_g \nabla \widetilde{Y}_g \tag{6}$$

where D_l and D_g are the liquid and gas diffusive coefficients. The tensor $\widehat{\tau}$ is the viscous stress tensor given by

$$\widehat{\tau} = 2\widetilde{\mu}\,\widetilde{B} \tag{7}$$

with

$$\widetilde{B}_{ij} = \frac{1}{2} \left(\frac{\partial \widetilde{U}_i}{\partial x_j} + \frac{\partial \widetilde{U}_j}{\partial x_i} \right) \tag{8}$$

and $\widetilde{\mu}$ is the molecular dynamic viscosity of the mixture.

The capillary stress tensor $\widehat{\tau}_c$ is expressed by

$$\widehat{\tau}_c = \gamma \|\nabla \widetilde{\alpha}_l\| \left(I - \frac{\nabla \widetilde{\alpha}_l}{\|\nabla \widetilde{\alpha}_l\|} \otimes \frac{\nabla \widetilde{\alpha}_l}{\|\nabla \widetilde{\alpha}_l\|} \right) \tag{9}$$

with

$$\alpha_l = \frac{\rho Y_l}{\rho_l} \tag{10}$$

Assuming that the heat flux is driven by the Fourier's law, $\widehat{\boldsymbol{J}}_e$ is given by

$$\widehat{\boldsymbol{J}}_e = -\widetilde{\lambda}_T \nabla \widetilde{T} + \widetilde{h}_l \widehat{\boldsymbol{J}}_l + \widetilde{h}_g \widehat{\boldsymbol{J}}_g \quad (11)$$

where h_l and h_g are, respectively, the specific enthalpies of liquid and gas, and λ_T is the thermal conductivity. The vector $\widehat{\boldsymbol{F}}_t$ is the turbulent flux vector resulting from the filtering, given by

$$\widehat{\boldsymbol{F}}_t = \begin{pmatrix} -\boldsymbol{J}_{l_t} \\ -\boldsymbol{J}_{g_t} \\ -\tau_t \\ -\boldsymbol{J}_{e_t} \end{pmatrix}$$

$$= \begin{pmatrix} -\widehat{\rho}(\widetilde{Y_l \boldsymbol{U}} - \widetilde{Y}_l \widetilde{\boldsymbol{U}}) \\ -\widehat{\rho}(\widetilde{Y_g \boldsymbol{U}} - \widetilde{Y}_g \widetilde{\boldsymbol{U}}) \\ -\widehat{\rho}(\widetilde{\boldsymbol{U} \otimes \boldsymbol{U}} - \widetilde{\boldsymbol{U}} \otimes \widetilde{\boldsymbol{U}}) \\ (\widehat{\tau - \widehat{\tau}_c}) \cdot \boldsymbol{U} - (\tau - \widehat{\tau}_c) \cdot \widetilde{\boldsymbol{U}} + (\widetilde{\rho e_t + p})\widetilde{\boldsymbol{U}} - (\widehat{\rho e_t + p})\boldsymbol{U} \end{pmatrix}$$

$$(12)$$

The turbulent terms introduced in the vector $\widehat{\boldsymbol{F}}_t$ require to be closed. The Boussinesq assumption is used to describe τ_t:

$$\tau_t = 2\mu_t \widetilde{B} - \frac{2}{3}\widehat{\rho}\mathrm{TKE} \cdot I \quad (13)$$

where μ_t is the turbulent viscosity and $\mathrm{TKE} = (\langle u_x''^2 \rangle + \langle u_y''^2 \rangle + \langle u_z''^2 \rangle)/2$, where u_x'', u_y'', and u_z'' are the velocity fluctuation components. The turbulent viscosity is based on the wall-attenuated Smagorinsky model [48] and is given by $\mu_t = \widehat{\rho}\min(C_s\Delta, \kappa l_w)^2 \sqrt{2I_B}$, where l_w is the distance from the nearest wall, $\kappa = 0.41$ is the Von Kàrmàn constant, C_s is set to 0.1, and I_B is given by

$$I_B = \sum_{ij} \widetilde{B}_{ij} \widetilde{D}_{ij} \quad (14)$$

The turbulent kinetic energy $\mathrm{TKE}_{\mathrm{SGS}}$ and the dissipation rate ϵ_{SGS} at the subgrid scale are approximated by $\mathrm{TKE}_{\mathrm{SGS}} = 2/0.3 \cdot C_s^2 \Delta^2 I_B$ and $\epsilon_{\mathrm{SGS}} = \mathrm{TKE}_{\mathrm{SGS}}^{3/2}/\Delta$. A turbulent diffusive closure is adopted for the turbulent fluxes $\boldsymbol{J}_{l_t}$ and $\boldsymbol{J}_{g_t}$. Introducing the turbulent diffusive coefficient D_t depending on the turbulent viscosity, the fluxes $\boldsymbol{J}_{l_t}$ and $\boldsymbol{J}_{g_t}$ are

$$\boldsymbol{J}_{l_t} = -\widehat{\rho}D_t \nabla \widetilde{Y}_l \quad (15)$$

and

$$\boldsymbol{J}_{g_t} = -\widehat{\rho}D_t \nabla \widetilde{Y}_g \quad (16)$$

The turbulent flux $\boldsymbol{J}_{e_t}$ is assumed to depend on the temperature gradient and is expressed by

$$\boldsymbol{J}_{e_t} = -\lambda_t \nabla \widetilde{T} + \widetilde{h}_l \boldsymbol{J}_{l_t} + \widetilde{h}_g \boldsymbol{J}_{g_t} + \tau_t \widetilde{\boldsymbol{U}} \quad (17)$$

where λ_t is the turbulent thermal conductivity, which is a function of μ_t, $\widetilde{Y}_l$, $\widetilde{Y}_g$, and $\widetilde{T}$.

A thermodynamic closure is necessary to link the density, the pressure, and the temperature of the mixture. Density is directly deduced from the conservative variables $\widehat{\rho} = \widehat{\rho}\widetilde{Y}_l + \widehat{\rho}\widetilde{Y}_g$. Introducing the gas volume fraction α_g and densities of pure phases ρ_l and ρ_g, density is written as $\widehat{\rho} = \widetilde{\alpha}_l \widehat{\rho}_l + \widetilde{\alpha}_g \widehat{\rho}_g$. For the liquid phase, a compressible liquid equation of state is used to link $\widehat{\rho}_l$ to the pressure and the temperature as $\widehat{\rho}_l = \rho_0[1 + \beta_0(\widehat{p} - p_0)]/[1 + \alpha_0(\widetilde{T} - T_0)]$, with β_0 being the isothermal compressibility of liquid and α_0 the isobaric dilatation coefficient, where subscript 0 refers to the reference state. For the gas phase, an ideal gas assumption is used for thermodynamic closure of the gas phase, yielding $\widehat{\rho}_g = \widetilde{p}/r_g \widetilde{T}$.

The numerical discretization relies on a finite volume method on a 3D unstructured mesh. The diffusive fluxes are calculated using a second-order cell-centered scheme. The convective fluxes are calculated using the Harten Lax Van Leer contact wave (HLLC) method based on the resolution of a Riemann problem [49]. A low-Mach-number version is used, which reduces numerical dissipation for incompressible flows. Cell-centered variables are interpolated to faces using a multislope method [43,50]. Unlike monoslope techniques classically used in finite-volume method [51], a scalar weighting of slopes, calculated at the different faces of a cell, is used to estimate the interpolated variables to each face, which improves the numerical accuracy. A Runge–Kutta second-order implicit scheme is used for temporal integration. A time step $\Delta t = 0.1$ μs is set for all simulations, yielding a maximum Courant–Friedrichs–Lewy number $\mathrm{CFL}_{\max} = \max(\|\boldsymbol{U}\| + c)\Delta t / \min(\delta_{\mathrm{grid}})$ below 1.8, where c is the speed of sound in water at 300 K.

B. Dispersed Phase Solver

The dispersed phase solver is the SPIREE solver from the CEDRE code [29]. It is based on an Eulerian calculation of droplets. The probability density function of droplet number n is calculated using the Williams–Boltzmann kinetic equation method [52]. Unlike the dense phase solver, no turbulence model is used in the dispersed phase solver. As a consequence, no filtering is made. The equations implemented in the solver are presented below. The velocity and temperature are assumed to be identical for every droplet in a cell. The vector of conservative variables is $\boldsymbol{Q}_d = (n, \alpha_d \rho_d, \alpha_d \rho_d \boldsymbol{U}_d, \alpha_d \rho_d e_{d_t})^t$, where α_d is the droplet volume fraction, ρ_d is their density, $\boldsymbol{U}_d$ is their velocity, and e_{d_t} is the total energy per unit of mass of the dispersed phase. The governing system for the dispersed phase is written as

$$\frac{\partial \boldsymbol{Q}_d}{\partial t} + \nabla \cdot \boldsymbol{F}_{C_d} = \boldsymbol{S}_{\mathrm{dis}} \quad (18)$$

where $\boldsymbol{F}_{C_d} = \boldsymbol{Q}_d \otimes \boldsymbol{U}_d$ is the convective flux vector. The diameter of generated droplets in the primary atomization region is uniformly equal to D_d. After primary atomization, the droplet diameter is susceptible to change due to fragmentation and coalescence mechanisms. However, choice is made to neglect these mechanisms. Therefore, this diameter is assumed to be constant in the simulations.

The source term $\boldsymbol{S}_{\mathrm{dis}}$ in Eq. (18) is based on the work of Le Touze [43] and Le Touze et al. [33]. It accounts for the mass, momentum, and energy transfers between the dispersed and dense phase solvers, due to atomization and impingement of droplets into the dense phase. It is expressed by

$$\boldsymbol{S}_{\mathrm{dis}} = \begin{pmatrix} S_a \dfrac{6}{\widehat{\rho}_l \pi D_d^3} - S_i \dfrac{6}{\rho_d \pi D_d^3} \\ S_a - S_i \\ n\boldsymbol{F}_d + S_a \widetilde{\boldsymbol{U}} - S_i \boldsymbol{U}_d \\ S_a\left(c_p(T_a) + \dfrac{1}{2}\widetilde{\boldsymbol{U}}^2\right) - S_i\left(c_p(T_d) + \dfrac{1}{2}\boldsymbol{U}_d^2\right) + n\boldsymbol{F}_d \cdot \boldsymbol{U}_d \end{pmatrix}$$

$$(19)$$

The atomization mass transfer S_a is expressed by $S_a = \widehat{\rho}\widetilde{Y}_l f_a \lambda_a(\widetilde{Y}_l)$, where f_a is a specific frequency for the atomization process and λ_a is a function depending on the liquid mass fraction. The frequency f_a accounts for the rate of the atomization process. In this study, f_a is the turbulent frequency, $f_a = \sqrt{2I_B}$, ensuring that the mass atomization rate is stronger as the flow is more turbulent. The function λ_a enables atomization only when the liquid mass fraction of the dense phase is negligible. This means that droplets cannot be formed inside a ligament, but only at the liquid–gas interface. The function λ_a is given by $\lambda_a = 1 - \tanh(a\widetilde{Y}_l^b)$, where a and b are constant values. During atomization, the initial ejected particle velocity $\boldsymbol{U}_d$ is the local velocity of the fluid $\widetilde{\boldsymbol{U}}$. The impingement mass

transfer S_i is based on the same formulation as S_a and is expressed by $S_i = \alpha_d \rho_d f_i \lambda_i(\widetilde{\alpha}_l, \alpha_d)$, where f_i is a specific frequency for the impingement mechanism and λ_i is a function of the liquid and droplet volume fraction. The latter is expressed by $\lambda_i = 1 - \tanh(-c_i \log_{10}[\max(\widetilde{\alpha}_l, \alpha_d)])$ with c_i a constant value. The frequency f_i is the inverse of the simulation integration step, $f_i = 1/\Delta t$, allowing all the droplets in a cell to be transferred to the dense liquid phase in one time step when $\lambda_i = 1$.

The drag force $\boldsymbol{F}_d$ exerted by the flow on a droplet is

$$\boldsymbol{F}_d = \frac{\pi D^2}{4} \rho C_d \|\widetilde{\boldsymbol{U}} - \boldsymbol{U}_d\|^2 (\widetilde{\boldsymbol{U}} - \boldsymbol{U}_d) \tag{20}$$

where C_d is the drag coefficient of the particle. It has different formulations depending on the droplet Reynolds number defined as $Re_d = \rho_d D_d \|\widetilde{\boldsymbol{U}} - \boldsymbol{U}_d\|/\mu_g$, where μ_g is the gas dynamic viscosity. According to the correlation of Schiller and Nauman [53], the corresponding drag coefficient is

$$C_d = \begin{cases} \dfrac{24}{Re_d} & \text{if } Re_d < 1 \\[2mm] \dfrac{24}{Re_d}(1 + 0.15 Re_d^{0.687}) & \text{if } 1 \le Re_d \le 1000 \\[2mm] 0.445 & \text{if } Re_d > 1000 \end{cases} \tag{21}$$

The source terms S_{dense} (2) and S_{dis} (19) enable mass, momentum, and energy transfers between the two solvers. The time steps used for the solvers are identical, allowing the source terms to be calculated at each iteration.

C. Synthetic-Eddy Method

The synthetic-eddy method SEM proposed by Jarrin et al. [40] and Jarrin [42] is used in this work to obtain a disturbed flow state at the nozzle exit, as in the work of Paysant et al. [54] with CEDRE [29]. It consists in injecting coherent structures through the water inlet boundary condition. For that purpose, an algorithm is employed to generate random eddies in a small box surrounding the inlet boundary and to calculate their position over time. A fluctuating velocity signal is then imposed at the water inlet boundary cells depending on the positions of the eddies.

1. Eddy Generation

The principle of the SEM algorithm is depicted in Fig. 3. To simplify, the scheme is presented for a 2-D geometry, but it applies to the three directions. A cylindrical box is defined as an extrusion of the inlet surface. It is located between $X = -\sigma$ and $X = +\sigma$, where $X = 0$ is the axial position of the inlet, and σ is the size of a turbulent spot. In the SEM box, N turbulent spots are inserted randomly and are convected at the velocity U_{inj} according to Taylor's frozen turbulence hypothesis. In practice, for all the simulations that follow, the exit velocity U_{ej} is equal to the inlet velocity U_{inj}, which is either 24.37 or 27.62 m $\cdot$ s^{-1}. When an eddy comes out of the box, it is randomly reinjected at the box inlet. Under such conditions, random eddies permanently cross the inlet boundary.
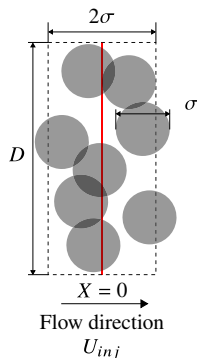

Fig. 3 Principle of eddy generation with SEM.

2. Turbulent Signal

Once eddies are generated and convected in the SEM box, they must be introduced into the dense phase solver. The following fluctuating velocity signal u'' is prescribed at a point on the water inlet surface $\boldsymbol{X} = (0, y, z)$ for each coordinate $i = (x, y, z)$:

$$u_i''(\boldsymbol{X}, t) = \frac{1}{\sqrt{N}} \sum_{j=1}^{3} W_{ij} \sum_{k=1}^{N} \epsilon_{ik} f_\sigma(\boldsymbol{X} - \boldsymbol{X}_k(t)) \tag{22}$$

where k is the index of a spot, $\boldsymbol{X}_k = (x_k, y_k, z_k)$ is the center of the spot k, and ϵ_{ik} is randomly equal to -1 or 1. The tensor W is given by

$$W = I_c U_{\text{inj}} \begin{pmatrix} w_x & 0 & 0 \\ 0 & w_y/\sqrt{2} & 0 \\ 0 & 0 & w_z/\sqrt{2} \end{pmatrix} \tag{23}$$

where w_x, w_y, and w_z are coefficients used to allocate the turbulent energy over the three space coordinates. They are set, respectively, to the values of 0.65, 0.35, and 0.35. The SEM intensity I_c is a coefficient that can be modified to adjust the intensity of the velocity fluctuations.

The function f_σ accounts for the influence of each eddy on the velocity depending on the distance between the center of the spot $\boldsymbol{X}_k(t)$ and the point $\boldsymbol{X}$:

$$f_\sigma(\boldsymbol{X} - \boldsymbol{X}_k(t)) = \sqrt{\frac{V_{\text{box}}}{\sigma^3}} f\left(\frac{x - x_k(t)}{\sigma}\right) f\left(\frac{y - y_k(t)}{\sigma}\right) f\left(\frac{z - z_k(t)}{\sigma}\right) \tag{24}$$

where the volume of the SEM box is $V_{\text{box}} = \sigma D(D/2 + 2\sigma)$. In this case, f is the tent function:

$$f(x) = \begin{cases} \sqrt{\dfrac{3}{2}}(1 - |x|) & \text{if } |x| < 1 \\[2mm] 0 & \text{otherwise} \end{cases} \tag{25}$$

The spots are convected at the velocity U_{inj} in the direction x. Thus, the evolution of the center of a spot k is determined by

$$\boldsymbol{X}_k(t + \Delta t) = \boldsymbol{X}_k(t) + \Delta t \boldsymbol{U}_{\text{inj}} \tag{26}$$

The total velocity at the inlet is finally

$$U_i(\boldsymbol{X}, t) = U_{\text{inj}} + u_i''(\boldsymbol{X}, t) \tag{27}$$

IV. Results

A. Preliminary SEM Results

A preliminary study is first conducted to calibrate the SEM and to analyze the flow inside the nozzle and at its exit. To reduce the simulation cost, runs are carried out on meshes with a refined area limited in the X direction, extending only to $X/D = 5$, as presented in Fig. 4. The simulations are carried out with the exit velocity $U_{\text{ej}} = 24.37$ m $\cdot$ s^{-1}. Two mesh sizes are tested, with grid sizes of $\delta_{\text{grid}} = 0.0229D$ and $\delta_{\text{grid}} = 0.0183D$, containing, respectively, 1.9 million cells and 3.5 million cells. The study is made from the results obtained after the flow transitory period. To cover the permanent regime, each run lasts approximately 85 h using 504 processors, during a physical time of 35 ms $= 195.2D/U_{\text{ej}}$. The SEM intensity I_c is set to 5% in this section.

1. SEM Parametric Study

The influence of the size σ and the number of spots, N, on the fluctuations at the nozzle inlet and exit is first studied. To reduce the simulation time cost, the LESs in this section are conducted using the coarser mesh only. It is assumed that similar results are obtained using the finer mesh. Three sizes of SEM spots, $\sigma_1 = 0.2D$, $\sigma_2 = 0.1D$,
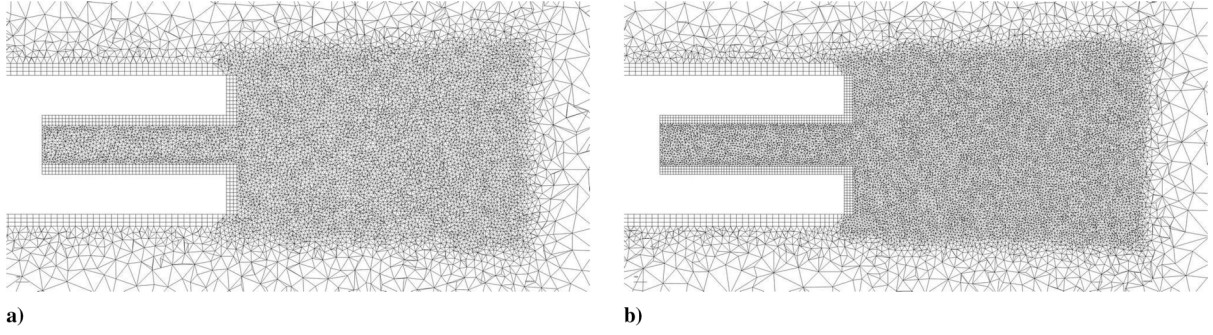
Fig. 4 Reduced meshes cuts: a) $\delta_{grid} = 0.0229D$; b) $\delta_{grid} = 0.0183D$.

and $\sigma_3 = 0.05D$, are tested for a number of spots in the box $N = 100$. The sizes of the spots are then $\sigma_1 = 8.73\delta_{grid}$, $\sigma_2 = 4.37\delta_{grid}$, and $\sigma_3 = 2.18\delta_{grid}$. The power spectral densities of U_x thus obtained at $r/D = 0.4$ at the nozzle inlet and exit are represented in Figs. 5a and 5b, as a function of the Strouhal number $St = fD/U_{ej}$, where f is the frequency. In this case, U_{ej} is equal to U_{inj} whose value is 24.37 m · s^{-1}. The power spectral densities (PSDs) are calculated using the Welch method with a 50% block overlapping over 10 blocks with a natural windowing. The spectra are plotted in dB/St, using a reference velocity of $U_0 = 1$ m · s^{-1}.

The spectra for the three sizes of spots at the nozzle inlet in Fig. 5a are all broadband. Most of the turbulent energy is contained between $St = 0.03$ and $St = 2$, and all the spectra collapse at $St \simeq 2$. The PSD for σ_1 decreases much faster than the ones for σ_2 and σ_3. Using the spot size σ_1 provides weaker fluctuating energy at high frequencies compared to the other sizes σ_2 and σ_3. However, there is not significant differences between the spectra for the sizes σ_2 and σ_3. At the nozzle exit in Fig. 5b, all the spectra are almost similar. The frequencies higher than $St = 1$ are filtered by the grid. It is concluded that the size of the turbulent spots does not significantly affect the fluctuations

obtained at the nozzle exit. The size $\sigma_3 = 0.05D$ is not chosen because of the high-frequency peaks seen at $St > 4$. The size $\sigma_2 = 0.1D$ is then selected for all the following simulations.

Three numbers of spots $N = 50$, $N = 100$, and $N = 200$ are also tested to evaluate their influence on the inlet and exit fluctuating velocity signals. The power spectral densities of U_x obtained at $r/D = 0.4$ with $\sigma = 0.1D$ for the grid size $\delta_{grid} = 0.0229D$ for these numbers of spots at the nozzle inlet and exit are represented in Figs. 6a and 6b. The spectra are almost similar. Therefore, the number of spots, N, does not have a significant influence on the fluctuating signal at the nozzle exit. The only difference is a peak at $St = 2$ at the inlet for $N = 200$ and a peak at $St = 4$ at the exit for $N = 50$. The value $N = 100$ is set in all the following simulations to have the most broadband spectrum.

2. Velocity Fluctuations Inside the Nozzle

The next simulations are carried out using $\sigma = 0.1D$ and $N = 100$. A field of the liquid Q criterion defined as $Q_l = \alpha_l^5 Q$ obtained for the grid spacing $\delta_{grid} = 0.0183D$ is represented in Fig. 7a. SEM spots can be seen inside the injector downstream of
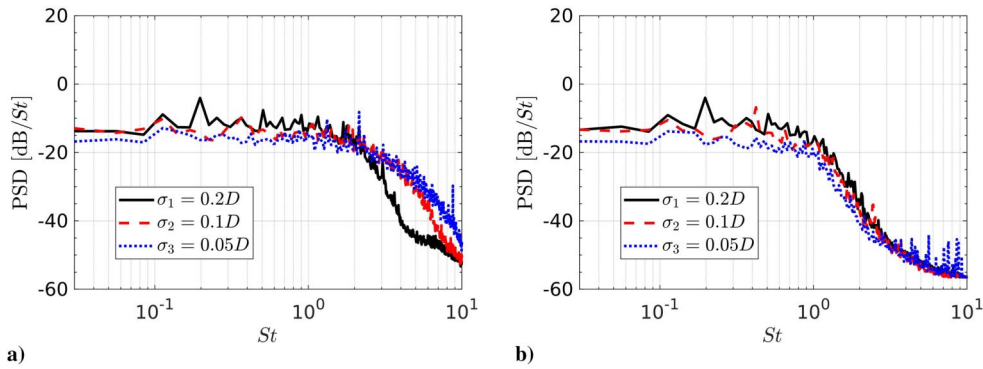
Fig. 5 Power spectral density of U_x obtained at $r/D = 0.4$ using SEM with $N = 100$ and $\sigma_1 = 0.2D$, $\sigma_2 = 0.1D$, and $\sigma_3 = 0.05D$: a) at the nozzle inlet; b) at the nozzle exit.
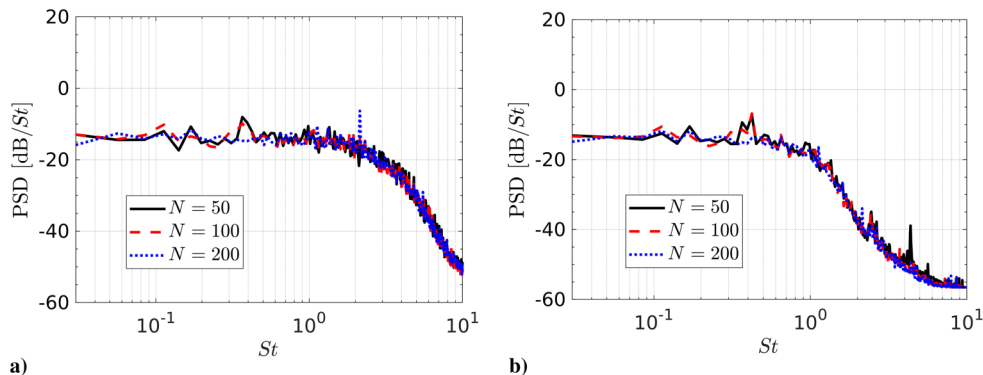

Fig. 6 Power spectral density of U_x obtained at $r/D = 0.4$ using SEM with $\sigma = 0.1D$ and $N = 50$, $N = 100$, and $N = 200$: a) at the nozzle inlet; b) at the nozzle exit.
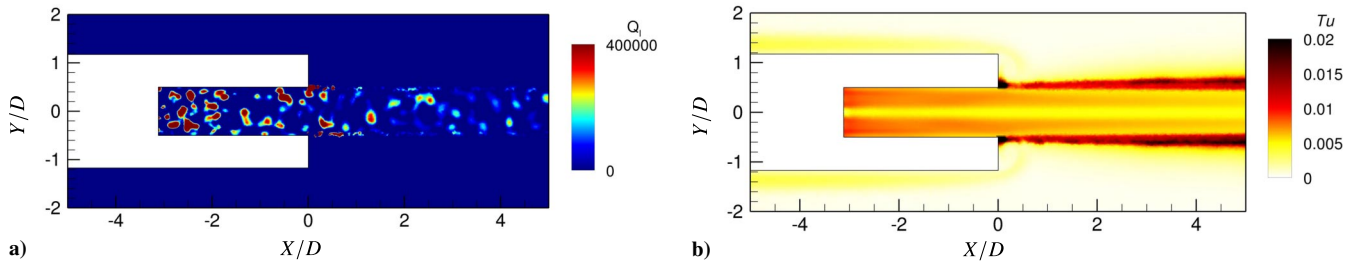
Fig. 7   Field in (X, Y) plane of a) Q_l criterion at $t = 111.5D/U_{ej}$, and b) turbulence intensity.

the water inlet, marked by maxima of Q_l. The field of the turbulence intensity $Tu = (2TKE/3)^{1/2}/U_{ej}$ is represented in Fig. 7b. The turbulence intensity is approximately equal to 1% inside the nozzle, and it is greater at the liquid–gas interface where it reaches almost 2%. To better quantify the turbulence intensity inside the nozzle, the axial variations of Tu, obtained at $r/D = 0.4$ for the two meshes, and at $r = 0$ and $r/D = 0.4$ for the finer mesh, are plotted in Figs. 8a and 8b. For the finer mesh in Fig. 8a, the turbulence intensity is equal to 0.9% near the nozzle inlet and decreases farther downstream, reaching a level of 0.65% at the nozzle exit, and a level of 0.55% for $X/D \geq 2$. Therefore, turbulence is dissipated in the liquid core with the axial distance. For the coarser mesh, the decrease rate of the turbulence intensity is the same as for the finer mesh, but the level near the water inlet is almost 0.15% lower. As a consequence, a better resolution of the mesh results in higher turbulence intensity in the liquid jet. For the finer mesh in Fig. 8b, the levels of turbulence intensity on the axis are almost half those at $r/D = 0.4$ in the injector near the nozzle inlet, which is due to the axisymmetric inlet condition implementation that modifies locally the spot size distribution for r tending to 0. As the development of instability waves at the liquid–gas interface is triggered by small perturbations around $r/D = 0.5$,

the low turbulent intensity level observed at the center of the jet should not affect the jet transition appreciably.

The power spectral densities of U_x obtained for the two grid sizes at $r/D = 0.4$ and $X = 0$, and for different axial positions at $r/D = 0.4$ using $\delta_{grid}/D = 0.0183$ are represented in Figs. 9a and 9b, respectively. For the coarser mesh in Fig. 9a, the cutoff frequency related to the grid size is observed around St $\simeq 1$, whereas it is higher and close to St $= 2.5$ for the finer mesh. The latter cutoff frequency corresponds to a wave discretized over 22 cells for the finer mesh, assuming a convection velocity of $U_{ej} = 24.37$ m · s^{-1}. In Fig. 9b, a broadband spectrum is seen to be generated at the inlet condition at $X/D = -3.12$, where it decreases for St ≥ 3. The components in the spectra at $X/D = -1.56$ and $X = 0$ collapse at St $\simeq 2.5$, sooner than those in the spectrum at $X/D = -3.12$, in line with the grid cutoff Strouhal number given above. The spectra at $X/D = -1.56$ and $X = 0$ are similar, indicating that the finer grid has no marked damping effect at $r/D = 0.4$ for $X/D \geq -1.56$.

These results show that disturbed inflow conditions are provided by the SEM for the parameters $N = 100$ and $\sigma = D/10$. The effects of the SEM on the nozzle exit conditions are investigated in the next section.
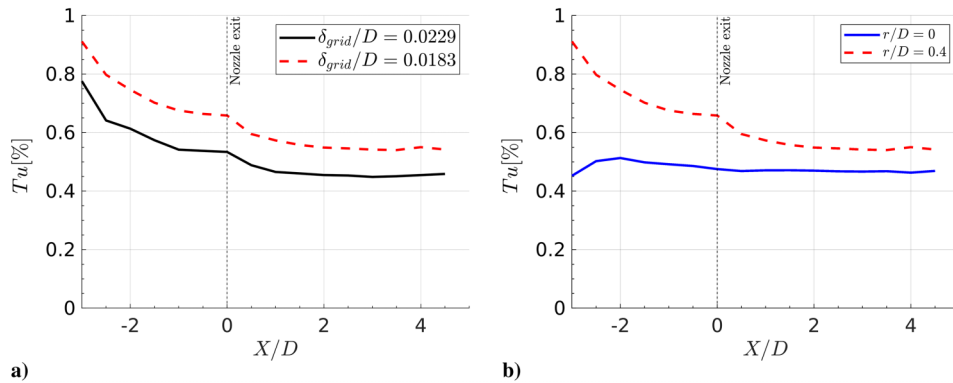

Fig. 8   Variations of the turbulent intensity with the axial distance to the nozzle exit: a) at $r/D = 0.4$ for the two meshes; b) at $r = 0$ and $r/D = 0.4$ for $\delta_{grid}/D = 0.0183$.
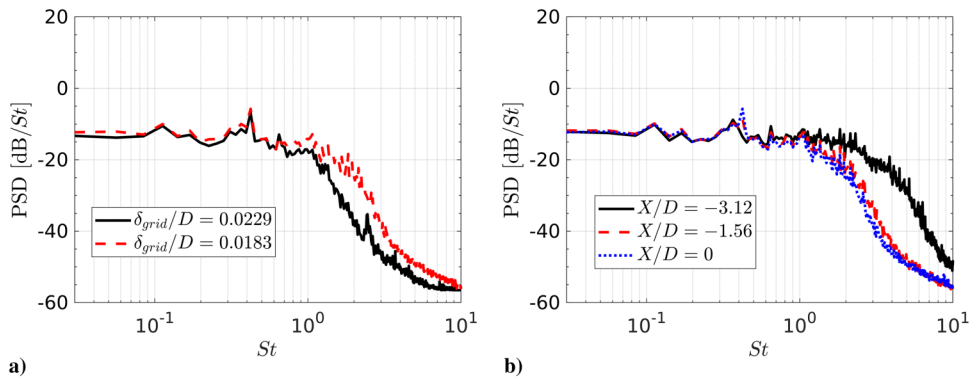

Fig. 9   Power spectral density of U_x obtained at $r/D = 0.4$ using SEM with $N = 100$ and $\sigma/D = 10$: a) at $X = 0$ for $\delta_{grid}/D = 0.0229$ and $\delta_{grid}/D = 0.0183$; b) for $\delta_{grid}/D = 0.0183$.

3. Nozzle Outlet Conditions

There are no available experimental data about the flow in the nozzle and at its exit, but a RANS simulation of the flow inside the nozzle with the full geometry presented in Fig. 1 has been conducted by Stevenin [27] and Stevenin et al. [28] to evaluate the velocity and the turbulent profiles at the nozzle exit. The results of the present LES are then compared to those of the RANS simulation in this region. The mean axial velocity profiles at the nozzle exit are plotted in Fig. 10a for the RANS simulation and for the LES using the two meshes. The LES data correspond to the values in each cell between $r = 0$ and $r/D = 0.5$. In all cases, the axial velocity is equal to the exit velocity U_{ej} between $r = 0$ and $r/D \simeq 0.35$. Then it decreases for $r/D > 0.35$ for the RANS simulation, corresponding to the boundary layer of the flow in the nozzle, whereas it is not true for the LES. For the LES profiles, only two or three cells are located in the boundary layer appearing in the RANS profile. The LES grids are then too coarse near the wall to discretize the flow in the boundary layer. The mean turbulent intensity Tu is plotted in Fig. 10b for the RANS simulation and the LES using the two meshes. From $r = 0$ to $r/D = 0.35$, the turbulent intensity in the RANS simulation is equal to 2%, and almost four times greater than the turbulent intensity in the LES. The peak of turbulent intensity in the boundary layer observed at $r/D \simeq 0.49$ is not captured by the LES computations, confirming that the LES grids are too coarse in this region.

It should be pointed out that taking into account the boundary layer is not an objective in this study. In this jet configuration, the transition of the jet into a turbulent regime is theoretically triggered by the amplification of KH instabilities due to the shear at the liquid–gas interface [15,55]. Even if the boundary layer is not captured by the LES, the presence of small perturbations near the liquid–gas interface just after the nozzle exit should be sufficient to seed the jet transition. The effects of the turbulence inside the boundary layer and of the boundary-layer thickness on the liquid–gas interface destabilization are not studied in this paper, but further results can be found in the works of Wu et al. [56] and Stahl et al. [46].

The following LES results are obtained for the two grid sizes using SEM, and for the finer grid without SEM. The mean radial profiles of

the axial velocity obtained for the LES at $X/D = 1$ are plotted in Fig. 11a. For the two grid sizes, the velocity decreases at $r/D \simeq 0.45$. It is minimum at $r/D \simeq 0.7$ for the coarser grid and $r/D \simeq 0.65$ for the finer grid. The vorticity-layer thickness δ_v, defined by $\delta_v = (U_{ej} - U_g)/(dU/dr_{\max})$, is equal to $\delta_v/D = 0.135$ for the coarser grid and $\delta_v/D = 0.119$ for the finer one. Compared to the grid size, the vorticity-layer thickness value is $\delta_v/\delta_{grid} = 5.90$ for the coarser grid and $\delta_v/\delta_{grid} = 6.50$ for the finer one. The vorticity-layer thickness is then strongly dependent of the mesh, most probably because of the diffuse interface method adopted in the calculations. Moreover, the profiles are similar between the LES with and without the SEM, suggesting that the SEM has negligible effects on the vorticity-layer thickness near the nozzle exit. The turbulent intensity profiles at $X/D = 1$ are plotted in Fig. 11b for the coarser and the finer mesh with SEM, and for the finer mesh without SEM. Using SEM, the turbulent intensity is equal to Tu $\simeq 0.5\%$ between $r = 0$ and $r/D = 0.4$, with a small hump at $r/D = 0.25$, and a second large bump is found at $r/D = 0.54$ with Tu $= 1.1\%$ for the finer mesh, and at $r/D = 0.57$ with Tu $= 1.25\%$ for the coarser mesh. These latter bumps are located in the vorticity layer identified in Fig. 11a. The turbulence intensity in LES without SEM is null for $r/D < 0.45$, and slightly increases at $r/D = 0.6$ to the value of 0.15%, but is significantly lower than the turbulence intensity for the LES with SEM. Therefore, the SEM strongly affects, as expected, the turbulence intensity in the liquid part of the jet, and especially the fluctuations in the liquid–gas interface region. The power spectral densities of the axial velocity in this area, at $r/D = 0.5$ and $X/D = 1$, are plotted in Fig. 12 for the two meshes with SEM. The spectra for the two grid sizes are close to each other and broadband. The use of the SEM generates initial fluctuations over a large frequency range in the liquid–gas mixing layer just after the nozzle exit. These fluctuations are necessary to excite the KH instabilities and the transition of the jet to a turbulent regime.

B. Analysis of the Dense Phase Instabilities

1. Jet Transition

Simulations of the jet are conducted with and without SEM using a mesh extending down to $40D$ from the nozzle exit with the finer grid
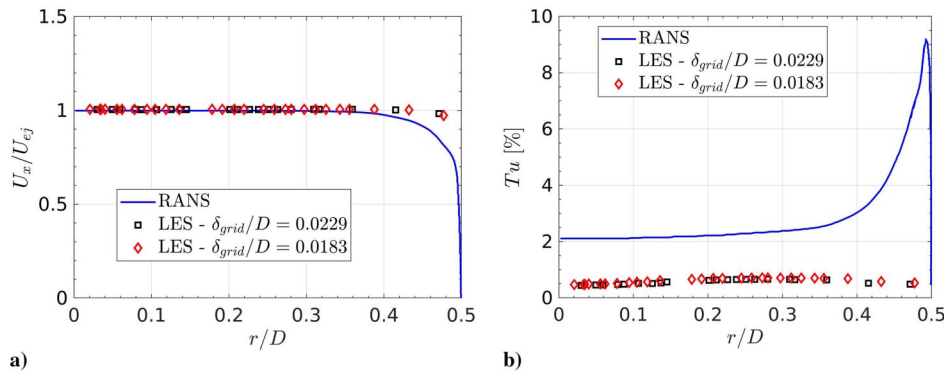

Fig. 10 Radial profiles at the nozzle exit of a) the axial velocity, and b) the turbulent intensity.
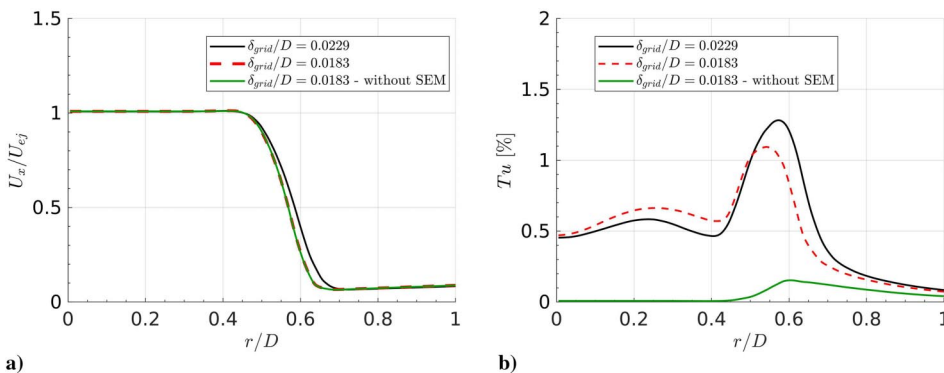

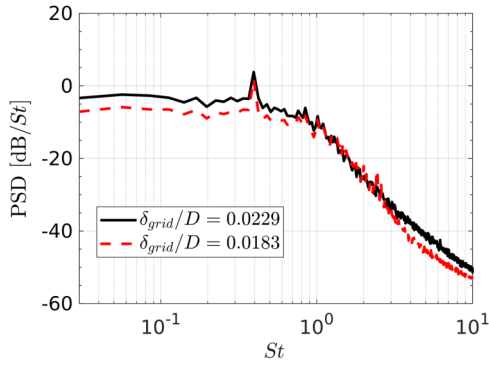**Fig. 11 Radial profiles at $X/D = 1$ of a) the axial velocity, and b) the turbulent intensity.**

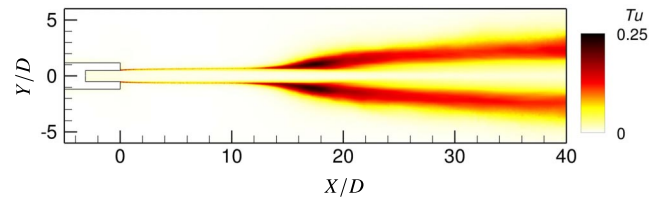**Fig. 12 Power spectral density of U_x obtained at $r/D = 0.5$ and $X/D = 1$ using SEM.**

Fig. 15 Mean turbulent intensity field in (X, Y) plane.

the simulation, comparisons with experimental data are presented in the next section.

size $\delta_{grid}/D = 0.0183$ illustrated in Fig. 2a. In this section, the simulations are carried out with the exit velocity $U_{ej} = 24.37$ m · s^{-1} and the SEM intensity of $I_c = 5\%$. To reach a time of $40D/U_{ej}$ in the permanent flow regime, each run lasts 385 h using 1512 processors, with no significant additional cost due to the use of SEM. The isosurface $\alpha_l = 0.15$ and streamlines obtained at $t = 20$ ms $= 111.5D/U_{ej}$ are represented in Fig. 13. Without SEM, in Fig. 13a, the jet remains laminar between $X = 0$ and $40D$. With SEM, in Fig. 13b, it becomes unstable at $X/D \simeq 15$, where small oscillations appear at the interface. Screenshots of the flow are unavailable in the experiments [27], but these waves can be seen in the analogous study of Hoyt and Taylor [12]. These oscillations are amplified as the distance from the nozzle exit increases. Therefore, the SEM has significant effects on the interface destabilization, and it is essential for the jet transition.

An isosurface of criterion $Q = 10^8$ is displayed in Fig. 14a. The eddy structures are mostly concentrated at $X/D \simeq 20$ and $r/D \simeq 1$. The isosurface of variable $Q_l = \alpha_l^5 Q$ is shown in Fig. 14b to highlight the eddies inside the liquid core. These structures are less visible as the distance from the nozzle exit increases, suggesting that they vanish in the jet and the mixing layer with the axial distance.

The turbulent intensities obtained in the (X, Y) plane are represented in Fig. 15. The levels are low for $X/D \leq 15$ in the laminar region of the jet. Further downstream, they reach maximum values of 25% between $X/D = 15$ and $X/D = 20$, during the jet transition. Finally, for $X/D \geq 20$, their values are almost equal to 15% in the turbulent region of the jet. The interface instabilities seen in Fig. 13b develop in the laminar part of the jet before $X/D = 15$ and their amplification leads to a transition to a turbulent regime for $X/D > 20$. To confirm that the jet transition is well reproduced by

2. Unstable Mode Identification

To identify the wave numbers of the interface instabilities, the properties of the fluctuations of the liquid–gas interface can be analyzed as in the work of Stevenin [27] based on the interface curvature defined as

$$C(s) = \frac{(dx/ds)(d^2y/ds^2) - (dy/ds)(d^2x/ds^2)}{((dx/ds)^2 + (dy/ds)^2)^{3/2}} \quad (28)$$

where s is the curvilinear abscissa of the interface, and x and y are the coordinates of a point at the interface in the plane (X, Y). In the work of Stevenin [27], the variations of the curvature were measured from camera snapshots. The spectra of the curvature fluctuations were found to be broadband, and the nondimensional wave numbers of the most energetic components were equal to $kD = 15.7$ at $X/D = 13$ and to $kD = 7.6$ at $X/D = 25$.

The power spectral densities of axial velocity computed from the LES with $U_{ej} = 24.37$ m · s^{-1} and $I_c = 5\%$ at $r/D = 0.5$ at $X/D = 0, 10, 20$ and 30 using the finer mesh are plotted in Fig. 16. At $X/D = 10$, a hump is clearly found around St $= 1.5$, which is 1.7 times smaller than the mesh cutoff frequency at St $= 2.5$ identified in Sec. IV.A.1, whereas no hump emerges at $X/D = 20$ and $X/D = 30$. An instability wave thus develops around St $\simeq 1.5$, leading to the jet transition. The wave number of this instability can be calculated from the temporal spectra using the phase velocity measured for St $= 1.5$ in the jet. For that, cross correlations are computed from velocity fluctuations obtained every $0.2D$ between $X/D = 10$ and $X/D = 30$, at $r/D = 0.5$, in two azimuthal planes. The phase velocity, averaged between $X/D = 10$ and $X/D = 30$, is thus found to be $U_C = 24.5$ m · s^{-1}, which is just slightly greater than the exit velocity of the liquid jet of 24.4 m · s^{-1}, and slightly greater than the theoretical phase velocity given by $U_{C_{th}} = (\sqrt{\rho_l}U_{ej} + \sqrt{\rho_g}U_g)/(\sqrt{\rho_l} + \sqrt{\rho_g}) = 23.5$ m · s^{-1} [57].
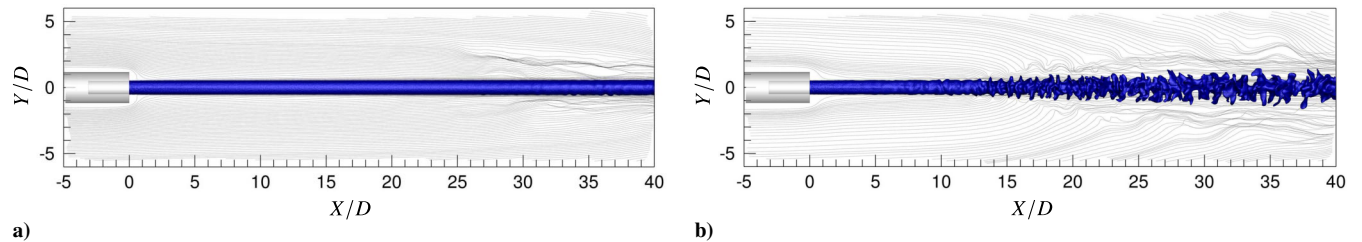

Fig. 13 Isosurface of volume fraction $\alpha_l = 0.15$ and streamlines at $t = 111.5D/U_{ej}$: a) without SEM; b) with SEM ($N = 100$, $\sigma/D = 10$).

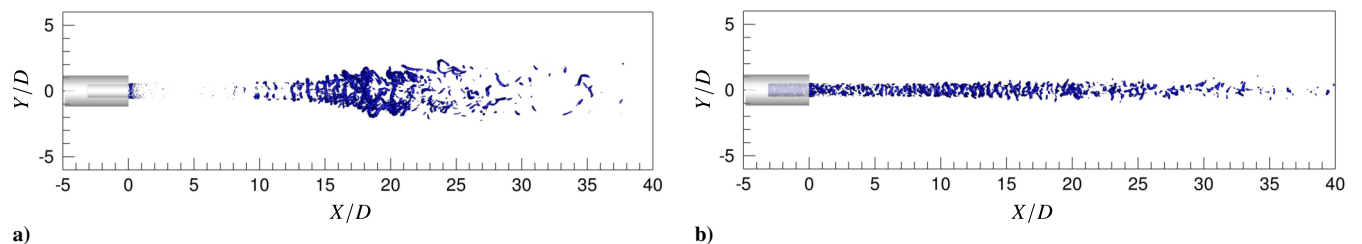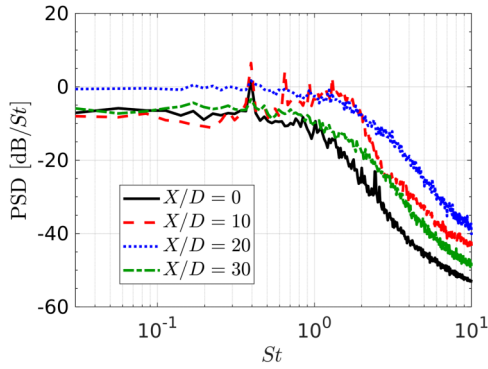**Fig. 14 Isosurface at $t = 111.5D/U_{ej}$ of a) $Q = 10^8$, and b) $Q_l = 10^5$.**

Fig. 16 Power spectral density of U_x at $r/D = 0.5$ for $\delta_{\mathrm{grid}}/D = 0.0183$ with $U_{\mathrm{ej}} = 24.37$ m · s^{-1} and $I_c = 5\%$.

The nondimensional wave number of the instability wave is expressed by $kD = 2\pi St U_{\mathrm{ej}}/U_C$. In the LES, its value is $kD = 9.4$, which is of the same order of magnitude as the wave number of the most energetic fluctuations measured in the experiment, equal to $kD = 15.7$ at $X/D = 13$ and $kD = 7.6$ at $X/D = 25$. Tonal spikes are also identified in Fig. 16 at $X/D = 10$, for $St = 0.4$, $St = 0.65$, $St = 0.9$, and $St = 1.5$. In particular, the peak at $St = 0.4$ is already present at $X = 0$ and is amplified with the jet transition. These tonal spikes' origin is not identified in this study, but probably arises from the numerical procedure.

To evaluate the influence of the grid size on the jet instability, the spectra of axial velocity obtained at $X/D = 10$ and $r/D = 0.5$ for the two grid sizes are plotted in Fig. 17, with $U_{\mathrm{ej}} = 24.37$ m · s^{-1} and $I_c = 5\%$. They are similar for the frequencies lower than $St = 1$, whereas the levels for the finer mesh are higher than the ones for the coarser mesh for $St > 1$. The most energetic instabilities are then not well computed by the coarser mesh.

The influence of the SEM intensity and the exit velocity on the jet instability is now evaluated using the finer mesh. For that, the PSDs of the axial velocity at $X/D = 10$ and $r/D = 0.5$ are plotted in Fig. 18 with the parameters [$U_{\mathrm{ej}} = 24.37$ m · s^{-1}, $I_c = 5\%$], [$U_{\mathrm{ej}} = 24.37$ m · s^{-1}, $I_c = 10\%$], and [$U_{\mathrm{ej}} = 27.62$ m · s^{-1}, $I_c = 5\%$]. For $U_{\mathrm{ej}} = 27.62$ m · s^{-1}, the spectrum is plotted for $X/D = 15$ rather than $X/D = 10$ because the transition occurs later than for $U_{\mathrm{ej}} = 24.37$ m · s^{-1}. This trend will be discussed in Sec. IV.B.3. All the spectra in Fig. 18 are very similar for $St > 0.4$. For $St < 0.4$, levels are slightly higher with $I_c = 10\%$ than with $I_c = 5\%$ for $U_{\mathrm{ej}} = 24.37$ m · s^{-1}. The SEM intensity then has an influence on the fluctuations at low frequencies, but has no significant effects at the middle and high frequencies, especially for the most energetic components around $St = 1.5$. With $I_c = 5\%$, the spectra for the two exit velocities are almost similar over the whole frequency range. Changing the SEM intensity or the exit velocity does not modify the value of the Strouhal number of the jet instability.

The radial profiles of the axial velocity for the same set of exit velocities and SEM intensities as in Fig. 18 at $X/D = 1$ and $r/D = $
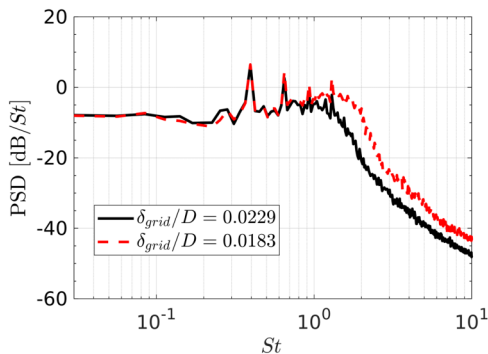

Fig. 17 Power spectral density of U_x at $X/D = 10$ and $r/D = 0.5$ for $\delta_{\mathrm{grid}}/D = 0.0229$ and $\delta_{\mathrm{grid}}/D = 0.0183$.
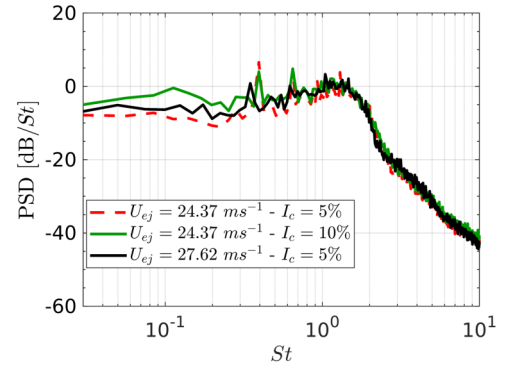

Fig. 18 Power spectral densities of U_x at $r/D = 0.5$ for $U_{\mathrm{ej}} = 24.37$ m · s^{-1} with the SEM intensity $I_c = 5\%$ and $I_c = 10\%$ at $X/D = 10$, and for $U_{\mathrm{ej}} = 27.62$ m · s^{-1} with the SEM intensity $I_c = 5\%$ at $X/D = 15$.

0.5 are plotted in Fig. 19. The profiles are all similar. As a consequence, the shear-layer thicknesses are nearly identical. The wave number of the jet instability, so as its Strouhal number, is expected to be proportional to the inverse of the vorticity-layer thickness $1/\delta_v$ at the nozzle exit [15,55]. This results in the same Strouhal number for the jet instability when changing the SEM intensity or the nozzle exit velocity.

3. Liquid–Gas Interface Position: Comparison with Experiments

Measuring the position of the mean liquid–gas interface is quite difficult because it relies on an arbitrary criterion. In the experiments of Stevenin [27], a shadowgraphy technique was used, and located the liquid–gas interface from a series of pictures recorded by a high-speed camera. The method is schematized in Fig. 20. On each picture perpendicular to the jet axis, the top and the bottom interfaces, referred to as interfaces 1 and 2 in Fig. 20, are detected using an image processing. The radius $R(X)$ is the distance of the interface from the axis at the abscissa X. A number of 500 pictures were processed, yielding 1000 data sets of $R(X)$.

Where the jet is laminar, a few diameters downstream of the nozzle exit, the liquid–gas interface is sharp and can be easily localized. However, when the jet is turbulent, the interface detection is less accurate. In that case, the interface position highly depends on the light threshold that is used in the measurements. In the present study, the interface is considered as diffuse. The diffusion can be either due to numerical dissipation or due to turbulence. The mean radius of the
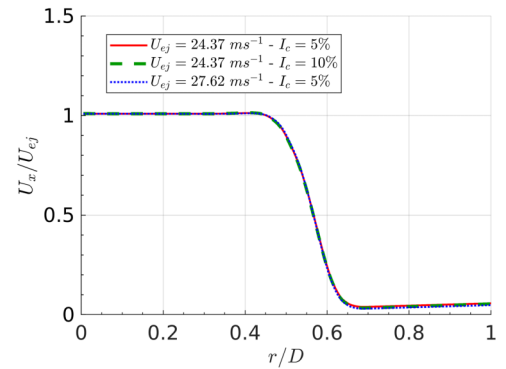

Fig. 19 Radial profiles of the axial velocity at $X/D = 1$ and $r/D = 0.5$ for $U_{\mathrm{ej}} = 24.37$ m · s^{-1} with the SEM intensity $I_c = 5\%$ and $I_c = 10\%$, and for $U_{\mathrm{ej}} = 27.62$ m · s^{-1} with the SEM intensity $I_c = 5\%$.
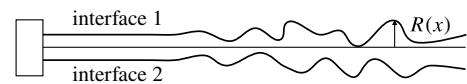

Fig. 20 Interface detection method.

liquid jet is evaluated from the LES mean field of liquid volume fraction using four different criteria with $U_{ej} = 24.37$ m · s^{-1} and $I_c = 5\%$ using the finer grid. It is compared with the corresponding experimental data in Fig. 21. In the first case, the jet radius is the position of the maximum volume fraction gradient max($\|\boldsymbol{grad}(\alpha_l)\|$). In the three other cases, the jet radius is defined as the position where the volume fraction is equal to the values of $\alpha_{l_\text{limit}} = 0.5, 0.15,$ and 0.1. Using the criteria max($\|\boldsymbol{grad}(\alpha_l)\|$) and $\alpha_{l_\text{limit}} = 0.5$, the mean jet radius in the LES matches the experimental one for $X/D < 10$, but significantly differs for $X/D > 10$ where turbulent structures appear. For $\alpha_{l_\text{limit}} = 0.15$, the experimental and LES results are close to each other down to $X/D = 40$. Similar trends are obtained for $\alpha_{l_\text{limit}} = 0.1$, but the jet radius in the LES is greater than the experimental one for $X/D > 20$ in that case. Therefore, the estimation of the jet radius in the LES depends weakly on the criterion for $X/D < 15$ but strongly for $X/D > 15$ where the jet is turbulent.

Another method to evaluate the mean jet radius, based on the same technique as the experimental measurements, is also used. It consists in analyzing instantaneous snapshots perpendicularly to the jet axis. In practice, the isosurface of $\alpha_l = 0.15$ is extracted from the instantaneous LES fields. At each position X, a slice of the isosurface is obtained and the maximum radius of the jet is determined in eight azimuthal planes. An example of the method is presented in Fig. 22, where the jet radii in the eight azimuthal sections are denoted as R_i, with $i = 1$ to 8. At each position X, the jet radius is the mean value of the eight radii R_i.

The mean radii of the liquid jet obtained between $X = 0$ and $40D$ in the LES with the interface detection method and from the mean liquid volume fraction $\alpha_{l_\text{limit}} = 0.15$ and in the experiment [27] are plotted in Fig. 23. The curves obtained from the LES data using the two methods are close to each other, and agree well with the experimental data. The mean radius is almost constant and equal to $0.5D$ for $X/D < 15$ in the laminar part of the jet. For $X/D > 25$, it does not vary much and is a bit higher than $0.6D$. In what follows, the method based on the mean liquid volume fraction $\alpha_{l_\text{limit}} = 0.15$ is used because it requires lesser storage resources and provides better converged results than the interface detection method.
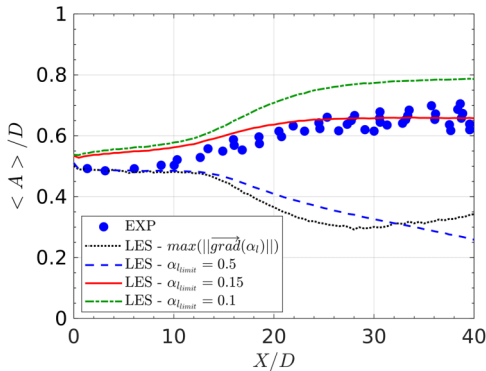

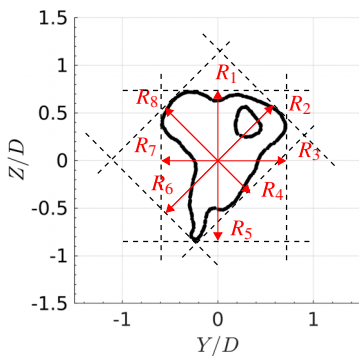**Fig. 21   Mean jet radius in the LES and in the experiment [27].**

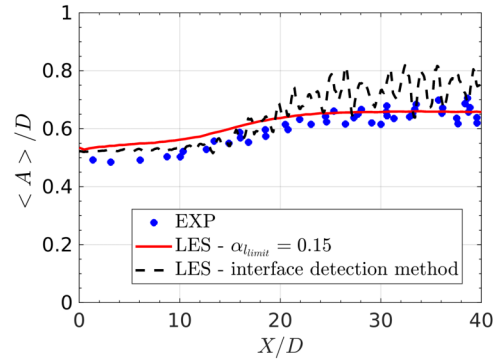**Fig. 22   Numerical interface detection method from a slice of the isosurface $\alpha_l = 0.15$.**

Fig. 23   Mean jet radius in the LES using the criterion $\alpha_{l_\text{limit}} = 0.15$ and using the interface detection method, and in the experiment [27].

The influence of the grid size, the SEM intensity, and the exit velocity on the mean jet radius is now studied. The jet radii obtained in the LES using the coarser mesh and the SEM intensity of $I_c = 5\%$ and using the finer mesh with $I_c = 5\%$ and $I_c = 10\%$ are plotted in Fig. 24a. The curves for the finer mesh using the two SEM intensities are superposed. The SEM intensity has then no effect on the axial variations of the mean jet radius. The curves for the two grid sizes with the SEM intensity $I_c = 5\%$ are also very similar. The position of the jet transition for the coarser grid is located shortly downstream of the one for the finer grid. The jet radii obtained in the LES using the finer mesh and the SEM intensity of 5% for $U_{ej} = 24.37$ m · s^{-1} and $U_{ej} = 27.62$ m · s^{-1} are represented in Fig. 24b. The curves are close to each other near the nozzle exit and at $X/D = 40$, but the position of the jet transition for $U_{ej} = 27.62$ m · s^{-1} is located downstream of the one for $U_{ej} = 24.37$ m · s^{-1}.

To explain this difference, the PSDs of the axial velocity at $X/D = 1$ and $r/D = 0.5$ are plotted in Fig. 25 for $U_{ej} = 24.37$ m · s^{-1} using $I_c = 5\%$ and $I_c = 10\%$, and for $U_{ej} = 27.62$ m · s^{-1} using $I_c = 5\%$. For $U_{ej} = 24.37$ m · s^{-1}, the levels are almost 5 dB lower for $I_c = 5\%$ than for $I_c = 10\%$ for St ≤ 0.8, whereas they are similar in both cases for St > 0.8. As a result, the initial fluctuations at the jet instability frequency at St $= 1.5$ have the same energy for both SEM intensities. Given that the spatial growth rate of the jet instability wave is proportional to $1/\delta_v$ [15,55], and that the vorticity-layer thicknesses near the nozzle exit are similar in both cases, the transition position does not vary with the SEM intensity. It can also be noticed that the PSD levels at low frequencies for St < 0.8 have not much influence on the mean jet radius variations and on the position of the jet transition.

Moreover, for $I_c = 5\%$ in Fig. 25, the levels are 5 dB lower for $U_{ej} = 27.62$ m · s^{-1} than for $U_{ej} = 24.37$ m · s^{-1} for St ≥ 0.8, whereas they are almost similar for St < 0.8 in both cases. As a result, the initial fluctuations at the instability frequency at St $= 1.5$ contain weaker energy for $U_{ej} = 27.62$ m · s^{-1}. Given that the vorticity-layer thicknesses are equal for both exit velocities, as seen in Fig. 19, the spatial growth rates are identical in both cases [15,55]. The jet transition for $U_{ej} = 27.62$ m · s^{-1} then occurs downstream of the one for $U_{ej} = 24.37$ m · s^{-1}. The position of the jet transition is then strongly dependent on the nozzle exit conditions, especially on the energy at the instability frequency as expected. In the study of Stevenin [27], the position of the jet transition is found to be closer to the nozzle exit for $U_{ej} = 27.62$ m · s^{-1} than for $U_{ej} = 24.37$ m · s^{-1}. The opposite behavior is obtained in the LES. It can be attributed to different nozzle exit conditions between the LES and the experiment, which can be due to either the nonresolution of the boundary layer inside the nozzle or an inappropriate SEM implementation when changing the exit velocity. Unfortunately, the vorticity-layer thickness and the PSD levels at the nozzle exit are unavailable in the experiment to confirm this.

The mean radial profiles of the liquid volume fraction obtained at $X/D = 210$ in the experiment [28] and at $X/D = 20, 30$ and 40 in the LES using the finer mesh are presented in Fig. 26. For the
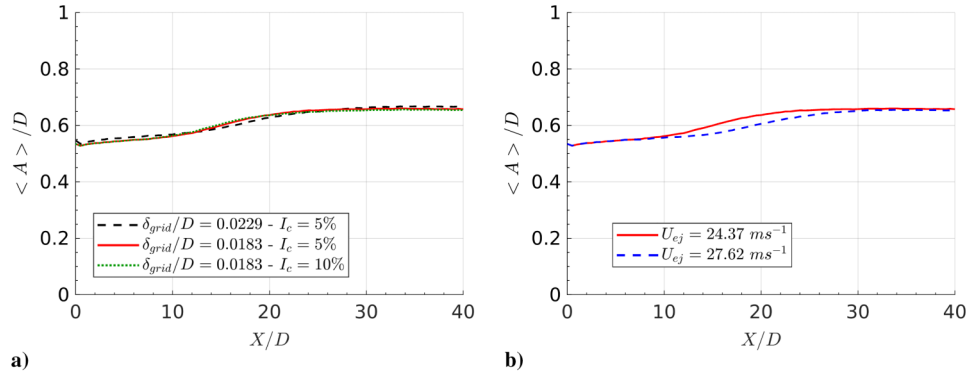
Fig. 24 Mean jet radius in the LES using $\alpha_{l_{\text{limit}}} = 0.15$: a) using the two grids with $I_c = 5\%$ and using the finer grid with $I_c = 10\%$; b) for the two exit velocities $U_{\text{ej}} = 24.37 \text{ m} \cdot \text{s}^{-1}$ and $U_{\text{ej}} = 27.62 \text{ m} \cdot \text{s}^{-1}$ with $I_c = 5\%$ using the finer grid.

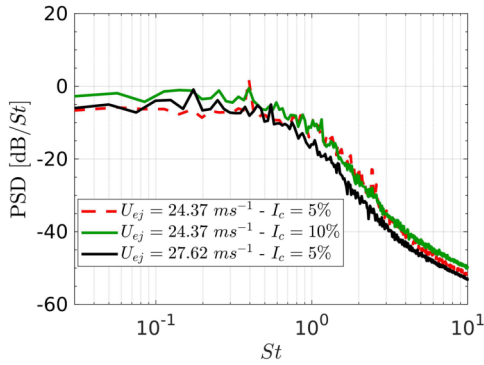**Fig. 25 PSD of the axial velocity at $X/D = 1$ and $r/D = 0.5$ for $U_{\text{ej}} = 24.37 \text{ m} \cdot \text{s}^{-1}$ with $I_c = 5\%$ and $I_c = 10\%$, and for $U_{\text{ej}} = 27.62 \text{ m} \cdot \text{s}^{-1}$ with $I_c = 5\%$, using the finer grid.**
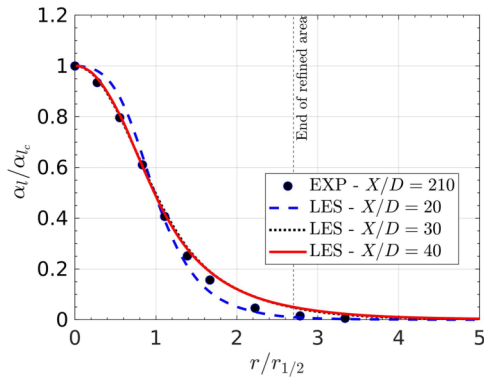

Fig. 26 Radial profiles of liquid volume fraction for the LES at $X/D = 20, 30,$ and 40 and for the experiments [28] at $X/D = 210$.

comparison, they are normalized using the liquid volume fraction at the center of the jet α_{l_c} and the jet half-width related to the liquid volume fraction $r_{1/2} = r(\alpha_l = \alpha_{l_c}/2)$. The LES profile at $X/D = 20$ is sharper than those at $X/D = 30$ and $X/D = 40$. At these two positions, they are similar to each other and match the experimental profile at $X/D = 210$. It can be deduced that, beyond $X/D = 30$, the radial profile of liquid volume fraction does not change significantly and is self-similar.

C. Atomization of the Liquid Jet

The results of the simulation using both the dense and the dispersed phase solvers are presented in this section. In the experiments [27,28], data about droplet characteristics such as size, velocity, and volume fraction are available only downstream of $X/D = 780$. As it would be too costly to simulate the jet down to that distance, it is not possible to directly compare simulation results with the

measurements. However, general trends can be highlighted. For instance, it has been shown in Stevenin et al. [28] that, at $X/D = 780$, the Sauter mean diameter of the droplets, given by the ratio between the total volume of the particles and their total area, is approximately 31.5 mm $= 0.34D$ on the center line, and decreases with the radial position to reach 1 mm $= 0.23D$ at $r/D = 13.5$. Thus, the droplets at the center are 15 times larger than the grid size using the coarser mesh, which should be enough to be discretized by the dense phase solver. For the simulation, the coupling strategy detailed in Sec. III.B is followed. For that, the diameter of the atomized droplets is evaluated using a method proposed in the work of Marmottant and Villermaux [15] based on the wave number of the interface instabilities found in Sec. IV.B.2.

1. Estimation of the Droplet Diameter

The KH instability waves at the interface initiate the development of an azimuthal RT instability [15]. The RT wavelength depends on the interface instability wavelength λ_i as [15]

$$\lambda_{\text{RT}} \simeq 2.45 \lambda_i \text{We}_{\lambda_i}^{-1/3} \qquad (29)$$

where $\text{We}_{\lambda_i} = \rho_g |U_{ej} - U_g|^2 \lambda_i/\sigma$ is the Weber number related to the interface instability wave.

The RT instability leads to the formation of ligaments whose diameter, for a sphere of equivalent volume, is equal to $D_{\text{lig}} = 0.23\lambda_{\text{RT}}$ [15]. These ligaments break up to eject droplets with a diameter equal to $D_d \simeq 0.4 D_{\text{lig}} = 0.092 \lambda_{\text{RT}}$ [15]. Given the Strouhal number of the instability wave at St $= 1.5$ in the simulated jet, yielding a wavelength of $\lambda_i = 2.815$ mm, it is found that $\lambda_{\text{RT}} \simeq 2.28$ mm. The droplet diameter is then $D_d \simeq 210$ μm, corresponding to $2.1\delta_{\text{grid}}$ for the coarser mesh, and $2.62\delta_{\text{grid}}$ for the finer mesh. Therefore, the droplets are too small to be calculated by the dense phase solver. This ensures that the atomized droplets are not captured simultaneously by the dense phase solver and by the dispersed phase solver. A more accurate method would be to use a sectional approach [58,59] to account for a more realistic particle size distribution in the spray. However, the simulation cost would be higher as it requires an additional set of equations for each new particle section. Thus, the monodispersed approach, with one droplet diameter, is retained in this work. In practice, the droplet diameter is arbitrary set in the simulation to 260 μm in order to ensure the continuity between the droplets and the dense phase.

2. Simulation Results with Atomization

Simulations are carried out with the atomization process using the coarser mesh to evaluate the model at a reduced cost. The runs last approximately 300 h using 924 processors. The exit velocity is $U_{\text{ej}} = 24.37 \text{ m} \cdot \text{s}^{-1}$ and the SEM intensity is set to $I_c = 5\%$. To investigate the influence of the re-absorption of the droplets by the dense phase on the flow, namely, the impingement phenomenon, calculations are performed with and without the impingement term in the model. This phenomenon can be suppressed simply by vanishing S_i in Eq. (19).
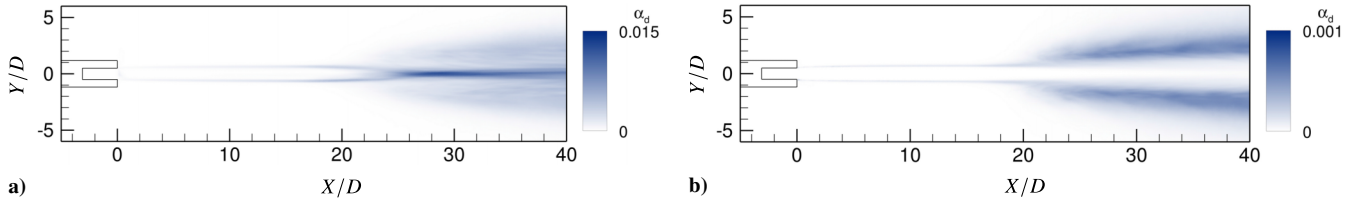
Fig. 27 Mean value of the liquid volume fraction of droplets in the (X, Y) plane: a) without impingement; b) with impingement in the model of Le Touze et al. [33].

The temperature of the atomized droplets is set to $T_a = 294.15$ K, assuming that the temperature of the dense liquid phase is equal to T_a. The constants a, b, and c_i of the atomization and impingement models defined in Sec. II.B are set, respectively, to 4, 2, and 2, following Le Touze et al. [33]. The mean liquid volume fractions of droplets obtained with and without impingement are shown in Fig. 27. In both cases, droplets are mostly present for $X/D \geq 20$, where the jet is turbulent. For $X/D < 20$, where the jet is not turbulent, a few droplets can be found at the liquid–gas interface at $r/D \simeq 0.5$. Further downstream, there is a significant amount of droplets on the center axis in the simulation without impingement, whereas the droplets are mostly located in the mixing layer in the simulation with impingement.

The radial profiles of the liquid volume fraction of droplets at $X/D = 30$ in Fig. 28 give more quantitative results about the droplet location. In the simulation without impingement, the liquid volume fraction of droplets has a local maximum on the center axis, whereas it is not the case for the turbulent intensity in Fig. 15. The liquid volume fraction is maximum at $r/D = 1.8$ in the liquid–gas turbulent mixing layer. On the contrary, in the simulation with impingement, there are no droplets on the jet axis, the maximum values are located around $r/D \simeq 2$, and the liquid volume fraction is almost five times smaller than in the simulation without impingement. To better understand these significant differences, the atomization and impingement rates are examined.

The mean values of the atomization rate S_a obtained in the simulation without impingement are shown in Fig. 29. Droplets are mostly formed in the shear layer between $X/D = 20$ and $X/D = 35$, and the atomization rate is zero on the jet axis. Therefore, the maximum concentration of droplets on the axis for $X/D > 20$ can be only
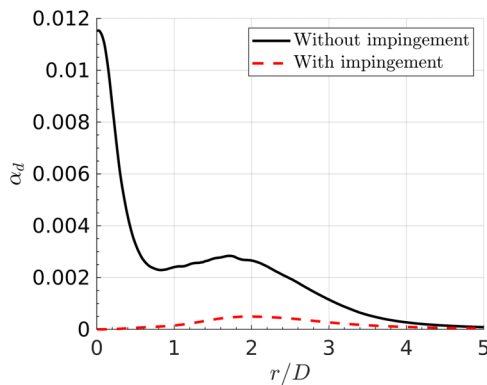

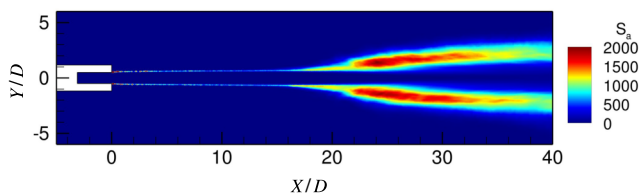**Fig. 28 Mean radial profiles of the liquid volume fraction of droplets at $X/D = 30$.**

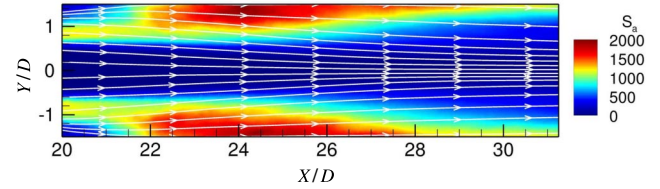**Fig. 29 Mean values of the atomization rate S_a [kg · s^{-1} · m^{-3}] in the plane (X, Y), for the simulation without impingement.**

Fig. 30 Mean values of the atomization rate S_a [kg · s^{-1} · m^{-3}] and streamlines of the droplets in the atomization region in the (X, Y) plane, simulation without impingement.
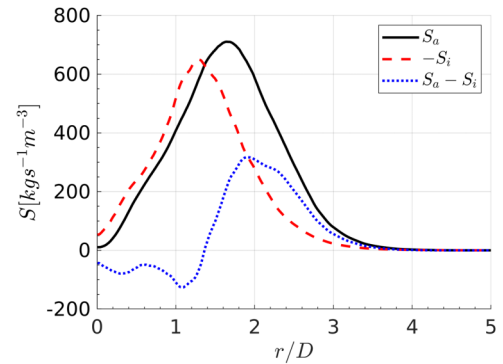

Fig. 31 Mean radial profiles of the atomization rate S_a, the impingement rate $-S_i$, and the total mass transfer rate $S_a - S_i$, in the simulation with atomization and impingement terms at $X/D = 30$.

explained by the droplet displacement from the shear layer, where they are created, toward the jet axis.

A zoom in the region where droplets are atomized is given in Fig. 30, where the values of the atomization rate and the streamlines of the droplets are represented. The streamlines are oriented toward the jet axis for $X/D > 22$, confirming that the droplets move from the shear layer to the axis.

The profiles of atomization and impingement rates obtained at $X/D = 30$ are plotted in Fig. 31. In both cases, the profiles are quite similar. The total mass transfer, relative to the dispersed phase, is negative for $r/D < 1.5$, whereas it is positive for $r/D \geq 1.5$. As a result, the droplets generated in the mixing layer that move toward the centerline are fully absorbed by the dense phase solver before they reach the center. The remaining amount of droplets that is ejected outward from the liquid jet is not absorbed by the dense liquid phase.

In the simulation with atomization and impingement, the large droplets and ligaments are calculated by the dense phase solver and are located near the jet axis, and the small droplets, calculated by the dispersed phase solver, are mostly located in the shear layer. The activation of the impingement model has a significant influence on the dispersed phase mean flow. It ensures that droplets do not stand in the dense liquid phase, and that the droplet volume fraction remains sufficiently low, by definition of the dispersed phase.

V. Conclusions

In the present study, the LES of a water jet exhausting into quiescent air has been carried out. The objective was to validate the calculation of the jet transition and the droplet generation based on an

experiment from the literature. The analysis of the dense phase regime shows that the jet transition occurs when fluctuations are generated with the synthetic-eddy method. This transition is governed by the development of an instability wave, marked by a hump at the Strouhal number St $= 1.5$ in the spectrum of the axial velocity at $X/D = 10$ and $r/D = 0.5$. The instability wave frequency is consistent with the one in the experiment. The variations of the mean jet radius, especially the position of the jet transition, are found to be in very good agreement with the experimental data. It is also shown that the position of the jet transition depends on the value of the fluctuating energy around the instability frequency near the nozzle exit.

The instability analysis has then been used to determine the diameter of the atomized droplets in the model. The simulation of the jet with both the dense and dispersed phase solvers shows that droplets are mostly generated in the turbulent regions of the flow. Moreover, the velocity of the droplets generated around $X/D = 25$ is slightly oriented toward the centerline. This leads to an accumulation of droplets around the jet axis for the simulation with atomization only. This effect is totally canceled if the impingement term is activated in the model, allowing droplets to be absorbed by the dense phase.

The validation of the method proposed in this paper against experimental data from the literature will permit to address the case of the water nozzles used on the MARTEL test bench [26] in future works. Unlike the nozzle used in this study, the nozzle at MARTEL ends with a converging section terminated by a lenticular exit. Adjustments of the parameters of the SEM used in this study should be made to take into account these differences.

Acknowledgments

References

[1] Bailly, C., and Bogey, C., "Propulsion System Noise: Jet," *Encyclopedia of Aerospace Engineering*, Vol. 6, 2010, 3522–3528.
https://doi.org/10.1002/9780470686652.eae335

[2] Tam, C. K. W., Golebiowski, M., and Seiner, J. M., "On the Two Components of Turbulent Mixing Noise from Supersonic Jets," *2nd AIAA/CEAS Aeroacoustics Conference*, AIAA Paper 1996-1716, 1996.
https://doi.org/10.2514/6.1996-1716

[3] McLaughlin, D. K., Morrison, G. L., and Troutt, T. R., "Experiments on the Instability Waves in a Supersonic Jet and Their Acoustic Radiation," *Journal of Fluid Mechanics*, Vol. 69, No. 1, 1975, pp. 73–95.
https://doi.org/10.1017/S0022112075001322

[4] Tam, C. K. W., and Tanna, H. K., "Shock Associated Noise of Supersonic Jets from Convergent-Divergent Nozzles," *Journal of Sound and Vibration*, Vol. 81, No. 3, 1982, pp. 337–358.
https://doi.org/10.1016/0022-460X(82)90244-9

[5] Seiner, J. M., and Yu, J. C., "Acoustic Near Field Properties Associated with Broadband Shock Noise," *AIAA Journal*, Vol. 22, No. 9, 1984, pp. 1207–1215.
https://doi.org/10.2514/3.8762

[6] Raman, G., "Advances in Understanding Supersonic Jet Screech: Review and Perspective," *Progress in Aerospace Sciences*, Vol. 34, Nos. 1–2, 1998, pp. 45–106.
https://doi.org/10.1016/S0376-0421(98)00002-5

[7] Zoppellari, E., and Juvé, D., "Reduction of Jet Noise by Water Injection," *3rd AIAA/CEAS Aeroacoustics Conference*, AIAA Paper 1997-1622, 1997.
https://doi.org/10.2514/6.1997-1622

[8] Norum, T. D., "Reductions in Multi-Component Jet Noise by Water Injection," *10th AIAA/CEAS Aeroacoustics Conference*, AIAA Paper 2004-2976, 2004.
https://doi.org/10.2514/6.2004-2976

[9] Ignatus, J. K., Sankaran, S., Kumar, R. A., and Satyanarayana, T. N. V., "Suppression of Jet Noise by Staged Water Injection During Launch Vehicle Lift-Off," *International Journal of Aeroacoustics*, Vol. 7, Nos. 3–4, 2008, pp. 223–242.
https://doi.org/10.1260/1475-472X.7.3.223

[10] Matas, J.-P., Marty, S., and Cartellier, A. H., "Experimental and Analytical Study of the Shear Instability of a Gas-Liquid Mixing Layer," *Physics of Fluids*, Vol. 23, No. 9, 2011, Paper 094112.
https://doi.org/10.1063/1.3642640

[11] Lawrence, G. A., Browand, F. K., and Redekopp, L. G., "The Stability of a Sheared Density Interface," *Physics of Fluids A: Fluid Dynamics*, Vol. 3, No. 10, 1991, pp. 2360–2370.
https://doi.org/10.1063/1.858175

[12] Hoyt, J. W., and Taylor, J. J., "Waves on Water Jets," *Journal of Fluid Mechanics*, Vol. 83, No. 1, 1977, pp. 119–127.
https://doi.org/10.1017/S0022112077001074

[13] Carpenter, J. R., Balmforth, N. J., and Lawrence, G. A., "Identifying Unstable Modes in Stratified Shear Layers," *Physics of Fluids*, Vol. 22, No. 5, 2010, Paper 054104.
https://doi.org/10.1063/1.3379845

[14] Varga, C. M., Lasheras, J. C., and Hopfinger, E. J., "Initial Breakup of a Small-Diameter Liquid Jet by a High-Speed Gas Stream," *Journal of Fluid Mechanics*, Vol. 497, No. 11, 2003, pp. 405–434.
https://doi.org/10.1017/S0022112003006724

[15] Marmottant, P., and Villermaux, E., "On Spray Formation," *Journal of Fluid Mechanics*, Vol. 498, July 2004, pp. 73–11.
https://doi.org/10.1017/S0022112003006529

[16] Lebas, R., Menard, T., Beau, P. A., Berlemont, A., and Demoulin, F. X., "Numerical Simulation of Primary Break-Up and Atomization: DNS and Modelling Study," *International Journal of Multiphase Flow*, Vol. 35, No. 3, 2009, pp. 247–260.
https://doi.org/10.1016/j.ijmultiphaseflow.2008.11.005

[17] Tanguy, S., and Berlemont, A., "Application of a Level Set Method for Simulation of Droplet Collisions," *International Journal of Multiphase Flow*, Vol. 31, No. 9, 2005, pp. 1015–1035.
https://doi.org/10.1016/j.ijmultiphaseflow.2005.05.010

[18] Chesnel, J., Reveillon, J., Ménard, T., and Demoulin, F., "Large Eddy Simulation of Liquid Jet Atomization," *Atomization and Sprays*, Vol. 21, No. 9, 2011, pp. 711–736.
https://doi.org/10.1615/AtomizSpr.2012003740

[19] Trontin, P., Vincent, S., Estivalezes, J.-L., and Caltagirone, J.-P., "An a Priori Study for the Modelling of Subgrid-Scale Phenomena in the Interaction Between a Liquid Sheet and a Decaying Turbulence," *FEDSM2008-55026. ASME 2008 Fluids Engineering Division Summer Meeting Collocated with the Heat Transfer, Energy Sustainability, and 3rd Energy Nano-Technology Conferences*, Volume 1: Symposia, Parts A and B, 2008.
https://doi.org/10.1115/FEDSM2008-55026

[20] Marchesse, Y., Gervais, Y., and Foulon, H., "Water Injection Effects on Hot Supersonic Jet Noise," *Comptes Rendus Mécaniques*, Vol. 330, No. 1, 2002, pp. 1–8.
https://doi.org/10.1016/S1631-0721(02)01418-3

[21] Fukuda, K., Tsutsumi, S., Shimizu, T., Takaki, R., and Ui, K., "Examination of Sound Suppression by Water Injection at Lift-Off of Launch Vehicles," *17th AIAA/CEAS Aeroacoustics Conference*, AIAA Paper 2011-2814, 2011.
https://doi.org/10.2514/6.2011-2814

[22] Capecelatro, J., and Buchta, D. A., "Direct Numerical Simulation of Noise Suppression by Water Injection in High-Speed Flows," *55th AIAA Aerospace Sciences Meeting*, AIAA Paper 2017-1700, 2017.
https://doi.org/10.2514/6.2017-1700

[23] Buchta, D. A., Shallcross, G., and Capecelatro, J., "Sound and Turbulence Modulation by Particles in High-Speed Shear Flows," *Journal of Fluid Mechanics*, Vol. 875, Jan. 2019, pp. 254–285.
https://doi.org/10.1017/jfm.2019.467

[24] Salehian, S., and Mankbadi, R. R., "Simulations of Rocket Launch Noise Suppression with Water Injection from Impingement Pad," *International Journal of Aeroacoustics*, Vol. 19, Nos. 3–5, 2020, pp. 207–239.
https://doi.org/10.1177/1475472X20930653

[25] Gueyffier, D., Li, J., Nadim, A., Scardovelli, R., and Zaleski, S., "Volume-of-Fluid Interface Tracking with Smoothed Surface Stress Methods for Three-Dimensional Flows," *Journal of Computational Physics*, Vol. 152, No. 2, 1999, pp. 423–456.
https://doi.org/10.1006/jcph.1998.6168

[26] Gely, D., Valière, J.-C., Lambaré, H., and Foulon, H., "Overview of Aeroacoustic Research Activities in MARTEL Facility Applied to Jet Noise," *Inter-Noise and Noise-Con Congress and Conference Proceedings*, Inst. of Noise Control Engineering, No. 6, 2006, pp. 1282–1290.

[27] Stevenin, C., "Étude de l'atomisation d'un jet d'eau haute vitesse. Application à l'irrigation par aspersion et à la pulvérisation," Ph.D. Thesis, Ecole Centrale Marseille, Marseille, France, 2012.

[28] Stevenin, C., Vallet, A., Tomas, S., Amielh, M., and Anselmet, F., "Eulerian Atomization Modeling of a Pressure-Atomized Spray for Sprinkler Irrigation," *International Journal of Heat and Fluid Flow*, Vol. 57, Feb. 2016, pp. 142–149.
https://doi.org/10.1016/j.ijheatfluidflow.2015.11.010

[29] Refloch, A., Courbet, B., Murrone, A., Villedieu, P., Laurent, C., Gilbank, P., Troyes, J., Tessé, L., Chaineray, G., Dargaud, J. B., Qué-merais, E., and Vuillot, F., "CEDRE Software," *AerospaceLab*, 2011, https://aerospacelab.onera.fr/CEDRE-Software.

[30] Yi, P., Yang, S., Habchi, C., and Lugo, R., "A Multicomponent Real-Fluid Fully Compressible Four-Equation Model for Two-Phase Flow with Phase Change," *Physics of Fluids*, Vol. 31, No. 2, 2019, Paper 026102.
https://doi.org/10.1063/1.5065781

[31] Zuzio, D., Thuillet, S., Rouzaud, O., Senoner, J.-M., Laurent, C., and Gajan, P., "Multi-Scale Simulation of the Atomization of a Liquid Jet in Cross-Flow in the Presence of an Acoustic Perturbation," *29th Conference on Liquid Atomization and Spray System*, ILASS-Europe, 2019.

[32] Rutard, N., Dorey, L.-H., Le Touze, C., and Ducruix, S., "Large-Eddy Simulation of an Air-Assisted Liquid Jet Under a High-Frequency Transverse Acoustic Forcing," *International Journal of Multiphase Flow*, Vol. 122, Jan. 2020, Paper 103144.
https://doi.org/10.1016/j.ijmultiphaseflow.2019.103144

[33] Le Touze, C., Dorey, L.-H., Rutard, N., and Murrone, A., "A Compress-ible Two-Phase Flow Framework for Large Eddy Simulations of Liquid-Propellant Rocket Engines," *Applied Mathematical Modelling*, Vol. 84, March 2020, pp. 265–286.
https://doi.org/10.1016/j.apm.2020.03.028

[34] Gaillard, P., Le Touze, C., Matuszewski, L., and Murrone, A., "Numeri-cal Simulation of Cryogenic Injection in Rocket Engine Combustion Chambers," *Journal Aerospace Lab*, No. 11, 2016, pp. 1–11, https://aerospacelab.onera.fr/al11/numerical-simulation-of-cryogenic-injection-in-rocket-engine-combustion-chambers.

[35] Magnaudet, J., Rivero, M., and Fabre, J., "Accelerated Flows Past a Rigid Sphere or a Spherical Bubble. Part 1. Steady Straining Flow," *Journal of Fluid Mechanics*, Vol. 284, June 1995, pp. 97–135.
https://doi.org/10.1017/S0022112095000280

[36] Tryggvason, G., Bunner, B., Esmaeeli, A., Juric, D., Al-Rawahi, N., Tauber, W., Han, J., Nas, S., and Jan, Y.-J., "A Front-Tracking Method for the Computations of Multiphase Flow," *Journal of Computational Physics*, Vol. 169, No. 2, 2001, pp. 708–759.
https://doi.org/10.1006/jcph.2001.6726

[37] Tanguy, S., "Développement d'une méthode de suivi d'interface. Appli-cations aux écoulements diphasiques," Ph.D. Thesis, Univ. de Rouen, Mont-Saint-Aignan, France, 2004.

[38] Sethian, J. A., "A Fast Marching Level Set Method for Monotonically Advancing Fronts," *Proceedings of the National Academy of Sciences*, Vol. 93, No. 4, 1996, pp. 1591–1595.
https://doi.org/10.1073/pnas.93.4.1591

[39] Enright, D., Fedkiw, R., Ferziger, J., and Mitchell, I., "A Hybrid Particle Level Set Method for Improved Interface Capturing," *Journal of Com-putational Physics*, Vol. 183, No. 1, 2002, pp. 83–116.
https://doi.org/10.1006/jcph.2002.7166

[40] Jarrin, N., Benhamadouche, S., Laurence, D., and Prosser, R., "A Synthetic-Eddy-Method for Generating Inflow Conditions for Large-Eddy Simulations," *International Journal of Heat and Fluid Flow*, Vol. 27, No. 4, 2006, pp. 585–593.
https://doi.org/10.1016/j.ijheatfluidflow.2006.02.006

[41] Jarrin, N., Prosser, R., Uribe, J.-C., Benhamadouche, S., and Laurence, D., "Reconstruction of Turbulent Fluctuations for Hybrid RANS/LES Simulations Using a Synthetic-Eddy Method," *International Journal of Heat and Fluid Flow*, Vol. 30, No. 3, 2009, pp. 435–442.
https://doi.org/10.1016/j.ijheatfluidflow.2009.02.016

[42] Jarrin, N., "Synthetic Inflow Boundary Conditions for the Numerical Simulation of Turbulence," Ph.D. Thesis, Univ. of Manchester, Man-chester, England, U.K., 2008.

[43] Le Touze, C., "Couplage entre modèles diphasiques à 'phases séparées' et à 'phase dispersée' pour la simulation de l'atomisation primaire en combustion cryotechnique," Ph.D. Thesis, Univ. Nice Sophia Antipolis, Nice, France, 2015.

[44] Reitz, R. D., *Atomization and Other Breakup Regimes of a Liquid Jet*, Univ. Microfilms International, Ann Arbor, MI, 1978, Chap. 1.

[45] Lasheras, J. C., and Hopfinger, E. J., "Liquid Jet Instability and Atomi-zation in a Coaxial Gas Stream," *Annual Review of Fluid Mechanics*, Vol. 32, No. 1, 2000, pp. 275–308.
https://doi.org/10.1146/annurev.fluid.32.1.275

[46] Stahl, M., Gnirb, M., Damaschke, N., and Tropea, C., "Laser Doppler Measurements of Nozzle Flow and Optical Characterisation of the Generated Spray," *20th ILASS–Europe Meeting*, ILASS-2005, Orléans, France, 2005, pp. 337–342.

[47] Baer, M. R., and Nunziato, J. W., "A Two-Phase Mixture Theory for the Deflagration-to-Detonation Transition (DDT) in Reactive Granular Materials," *International Journal of Multiphase Flow*, Vol. 12, No. 6, 1986, pp. 861–889.
https://doi.org/10.1016/0301-9322(86)90033-9

[48] Smagorinsky, J., "General Circulation Experiments with the Primitive Equations. I. The Basic Experiment," *Monthly Weather Review*, Vol. 91, No. 3, 1963, pp. 99–164.
https://doi.org/10.1175/1520-0493(1963)091<0099:GCEWTP>2.3.CO;2

[49] Toro, E. F., Spruce, M., and Speares, W., "Restoration of the Contact Surface in the HLL-Riemann Solver," *Shok Waves*, Vol. 4, No. 1, 1994, pp. 25–34.
https://doi.org/10.1007/BF01414629

[50] Le Touze, C., Murrone, A., and Guillard, H., "Multislope MUSCL Method for General Unstructured Meshes," *Journal of Computational Physics*, Vol. 284, March 2015, pp. 389–418.
https://doi.org/10.1016/j.jcp.2014.12.032

[51] Haider, F., Courbet, B., and Croisille, J.-P., "A High-Order Interpolation for the Finite Volume Method: The Coupled Least Squares Reconstruction," *Computers and Fluids*, Vol. 176, Nov. 2018, pp. 20–39.
https://doi.org/10.1016/j.compfluid.2018.09.009

[52] Williams, F. A., "Spray Combustion and Atomization," *Physics of Fluids*, Vol. 1, No. 6, 1958, pp. 541–545.
https://doi.org/10.1063/1.1724379

[53] Schiller, L., and Naumann, Z., "A Drag Coefficient Correlation," *Zeitschrift des Vereins Deutscher Ingenieure*, Vol. 77, 1935, pp. 77–318.

[54] Paysant, R., Laroche, E., Troyes, J., Donjat, D., Millan, P., and Buet, P., "Scale Resolving Simulations of a High-Temperature Turbulent Jet in a Cold Crossflow: Comparison of Two Approaches," *International Jour-nal of Heat and Fluid Flow*, Vol. 92, Dec. 2021, Paper 108862.
https://doi.org/10.1016/j.ijheatfluidflow.2021.108862

[55] Eggers, J., and Villermaux, E., "Physics of Liquid Jets," *Reports on Progress in Physics*, Vol. 71, No. 3, 2008, Paper 036601.
https://doi.org/10.1088/0034-4885/71/3/036601

[56] Wu, P.-K., Miranda, R. F., and Faeth, G. M., "Effects of Initial Flow Conditions on Primary Breakup of Nonturbulent and Turbulent Liquid Jets," *32nd Aerospace Sciences Meeting and Exhibit*, AIAA Paper 1994-056, 1994.
https://doi.org/10.1615/AtomizSpr.v5.i2.40

[57] Dimotakis, P. E., "Two-Dimensional Shear-Layer Entrainment," *AIAA Journal*, Vol. 24, No. 11, 1986, pp. 1791–1796.
https://doi.org/10.2514/3.9525

[58] Tambour, Y., "A Lagrangian Sectional Approach for Simulating Droplet Size Distribution of Vaporizing Fuel Sprays in a Turbulent Jet," *Com-bustion and Flame*, Vol. 60, No. 1, 1985, pp. 15–28.
https://doi.org/10.1016/0010-2180(85)90115-4

[59] Greenberg, J. B., Silverman, I., and Tambour, Y., "On the Origins of Spray Sectional Conservation Equations," *Combustion and Flame*, Vol. 93, No. 1, 1993, pp. 90–96.
https://doi.org/10.1016/0010-2180(93)90085-H

P. G. Tucker
Associate Editor